

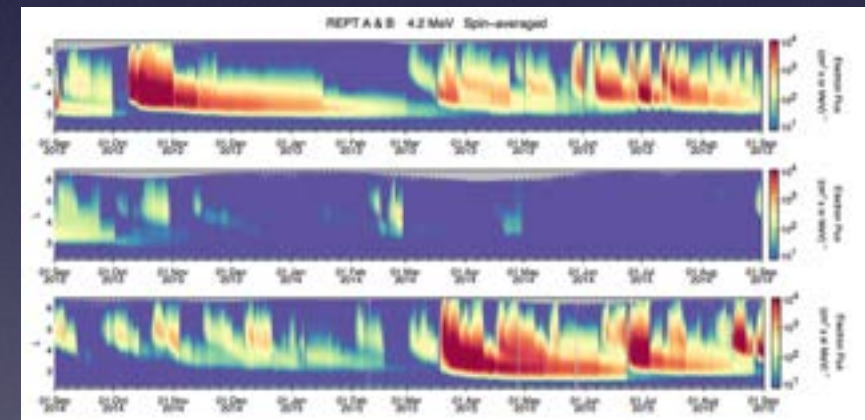
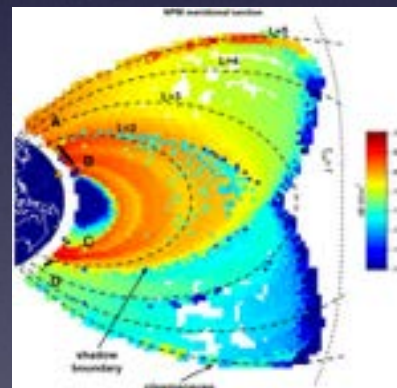
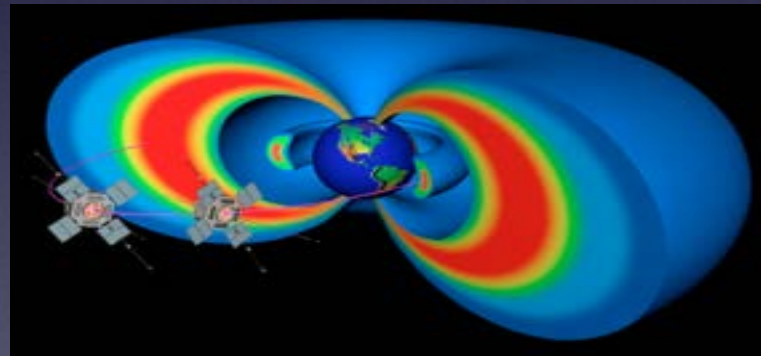
Anthropogenic Space Weather (Human Effects on Geospace)

Dr. P. J. Erickson, W1PJE
MIT Haystack Observatory

T.I. Gombosi · D.N. Baker · A. Balogh

J.D. Huba · L.J. Lanzerotti · J. C. Foster · J. M. Albert · J. F. Fennell

E. V. Mishin · M. J. Starks · A. N. Jaynes · X. Li · S. G. Kanekal · C. Kletzing
and a cast of many others



Space Weather Knowledge Exchange
Milton Keynes, UK
13 October 2017

SWL leads to a career in Ionospheric Radar and Physics

Hallicrafters SX-110 (1962)



6SG7 RF Amp, 6SA7 Converter, 6SG7 1st IF Amp, 6SK7 2nd IF Amp, 6SC7 Audio Amp/BFO, 6K6GT Audio Output, 6H6 Detector/ANL/AVC and 5Y3GT Rectifier.

**MIT Haystack Observatory Complex
Westford, Massachusetts
Established 1956**

Haystack Observatory

**Radio Astronomy
Atmospheric Science
Space Surveillance
Radio Science
Education and Public Outreach**

**Millstone Hill
Observatory**

Millstone Hill Radar

**Firepond Optical
Facility**

Millstone Hill 440 MHz Incoherent Scatter Radar

MISA 150-ft steerable antenna

transmitter →

Fixed zenith-pointing dish



Anthropogenic Space Weather (Human Effects on Geospace)

Outline:

- **Natural vs. Anthropogenic (e.g. QRN vs. QRM)**
- **High Altitude Nuclear Explosions (HANE):**
 - **EMP**
 - **Artificial Radiation Belts**
 - **Satellite Damage**
 - **Geomagnetic Signals**
- **VLF Human Transmissions and their effects on the Radiation Belts**

Gombosi, T.I., D. N. Baker, A. Balogh, P. J. Erickson, J. D. Huba, and L. J. Lanzerotti (2017), Anthropogenic Space Weather, *Space Sci. Rev.*, doi:10.1007/s11214-017-0357-5.

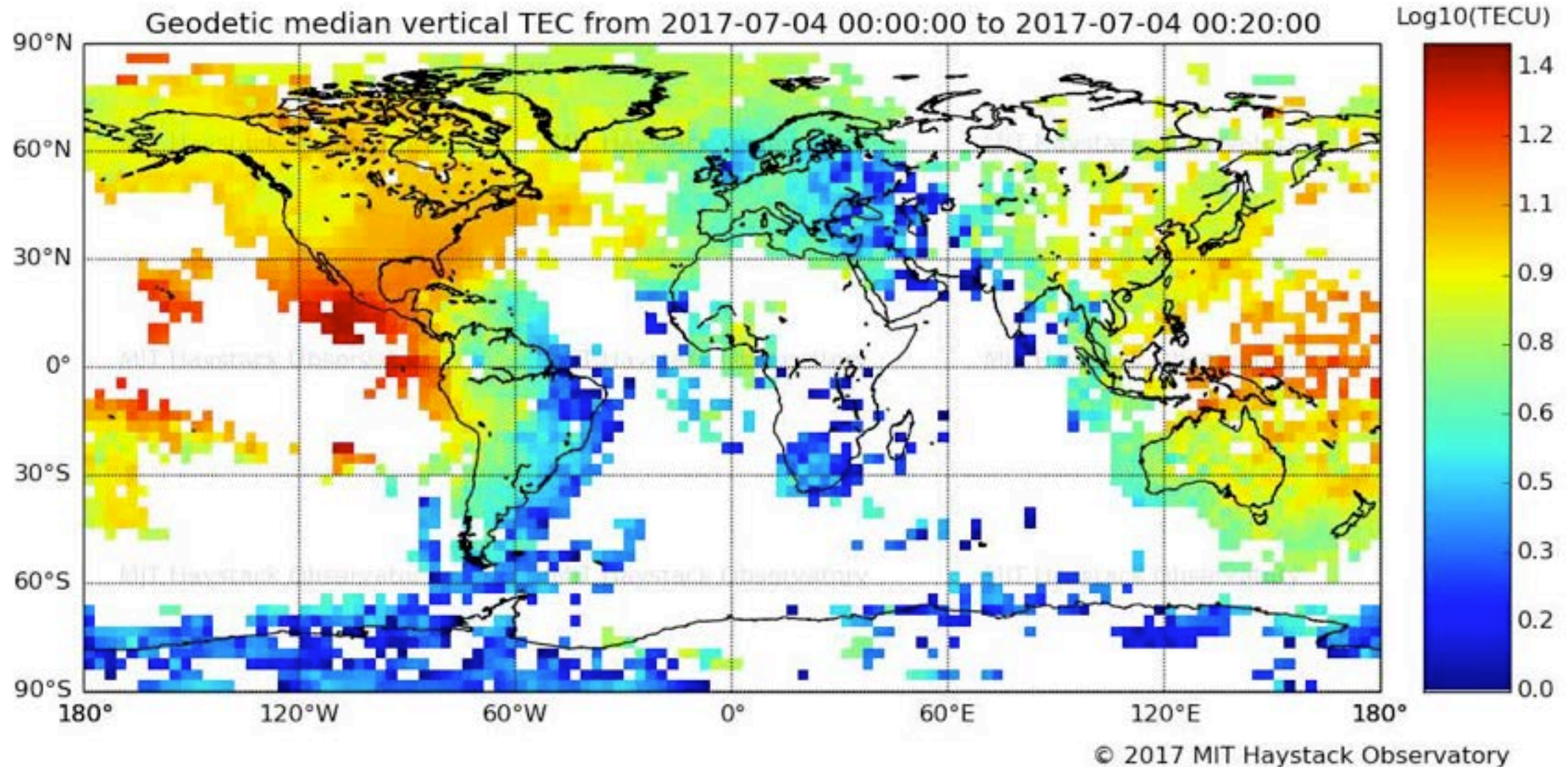
Foster, J. C., P. J. Erickson, D. N. Baker, A. N. Jaynes, E. V. Mishin, J. F. Fennel, X. Li, M. G. Henderson, and S. G. Kanekal (2016), Observations of the impenetrable barrier, the plasmopause, and the VLF bubble during the 17 March 2015 storm, *J. Geophys. Res. Space Physics*, 121, 5537–5548, doi:10.1002/2016JA022509.



Space Weather Knowledge Exchange
Milton Keynes, UK
13 October 2017

The Ionosphere Is Naturally Complex

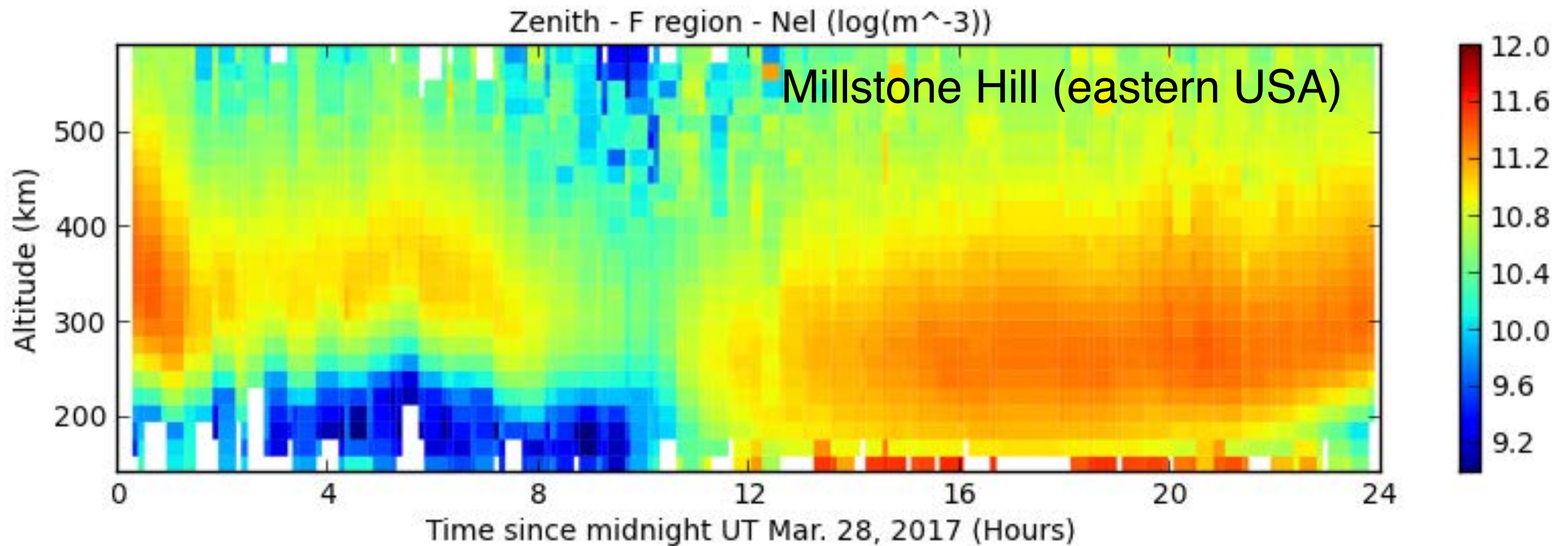
(red = more electrons, blue = less)



Varies in Space, Time: Natural Space Weather

The Ionosphere Is Naturally Complex

(red = more electrons, blue = less)



Varies in Altitude: Natural Space Weather

Table 1 List of high-altitude nuclear explosions (Wikipedia Contributors 2016)

Designation	Country	Date	Altitude	Yield (kt)
Yucca	USA	Apr 28, 1958	26 km	1.7
Teak	USA	Aug 1, 1958	77 km	3.8×10^3
Orange	USA	Aug 12, 1958	43 km	3.8×10^3
Argus I	USA	Aug 27, 1958	200 km	1.7
Argus II	USA	Aug 30, 1958	240 km	1.7
Argus III	USA	Sep 6, 1958	540 km	1.7
Test#88	USSR	Sep 6, 1961	23 km	10.5
Test#115	USSR	Oct 6, 1961	41 km	40
Test#127	USSR	Oct 27, 1961	150 km	1.2
Test#128	USSR	Oct 27, 1961	300 km	1.2
Starfish Prime	USA	Jul 9, 1962	400 km	1.4×10^3
Checkmate	USA	Oct 20, 1962	147 km	7
Test#184	USSR	Oct 22, 1962	290 km	300
Bluegill Triple Prime	USA	Oct 26, 1962	50 km	410
Test#187	USSR	Oct 28, 1962	150 km	300
Kingfish	USA	Nov 1, 1962	97 km	410
Test#195	USSR	Nov 1, 1962	59 km	300

High Altitude Nuclear Explosions (HANE)



Treaty Banning Nuclear Weapon Tests in the Atmosphere, in Outer Space and Under Water

BUREAU OF ARMS CONTROL, VERIFICATION, AND COMPLIANCE

Signed at Moscow August 5, 1963
Entered into force October 10, 1963

Ratified 20 Oct 1963



Fig. 1 From *left to right*, the Orange, Teak, Kingfish, Checkmate, and Starfish high-altitude nuclear tests conducted in 1958 and 1962 by the United States near Johnston Island in the mid-Pacific (from Foster et al. 2008)

High-altitude nuclear EMP (HEMP)

Fig. 2 The various phases of a generic HEMP signal (from Savage et al. 2010). For comparison, we also show a typical electromagnetic signal from lightning

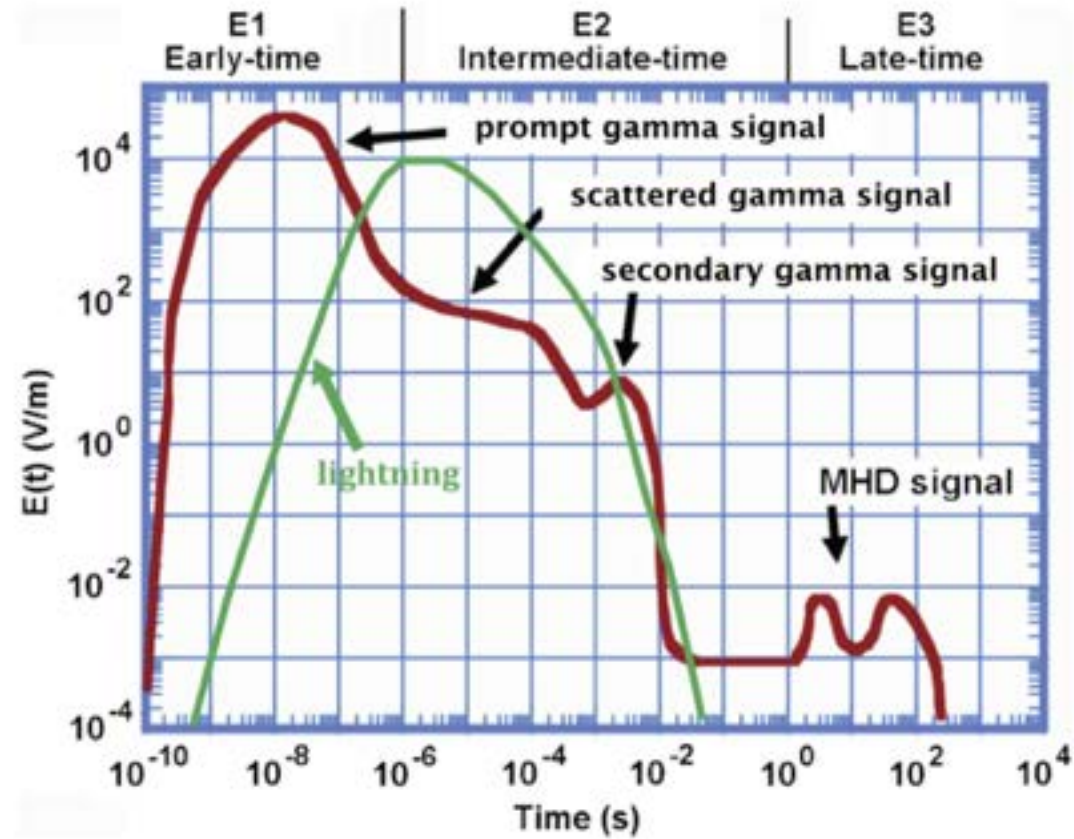
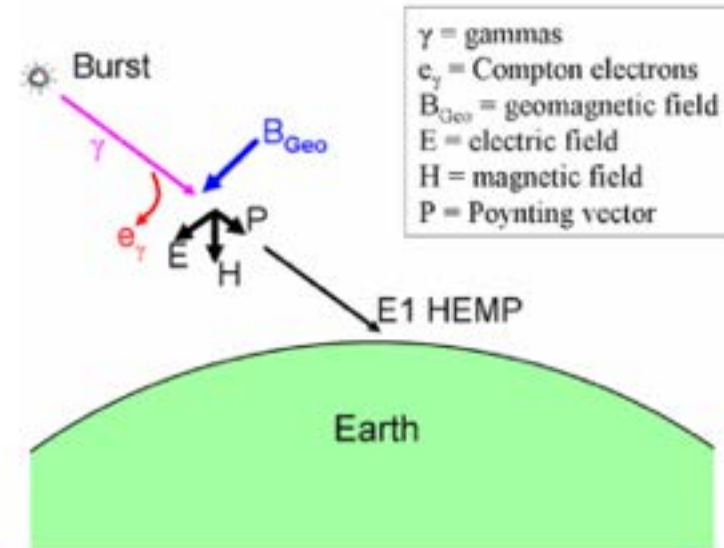


Fig. 3 General basis of the E1 HEMP generation process. Gammas from the nuclear burst interact with the upper atmosphere generating Compton electrons, which are turned in the Earth's geomagnetic field, and produce a transverse current that radiates an EM pulse towards the Earth (from Savage et al. 2010)



High-altitude nuclear EMP (HEMP)

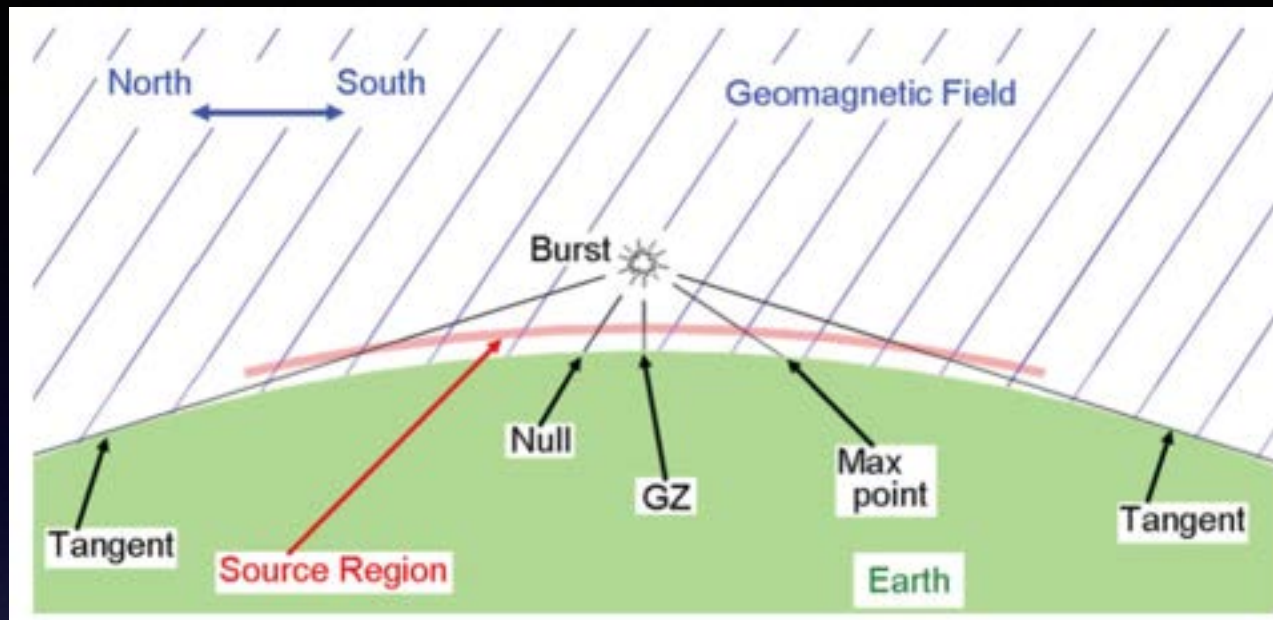


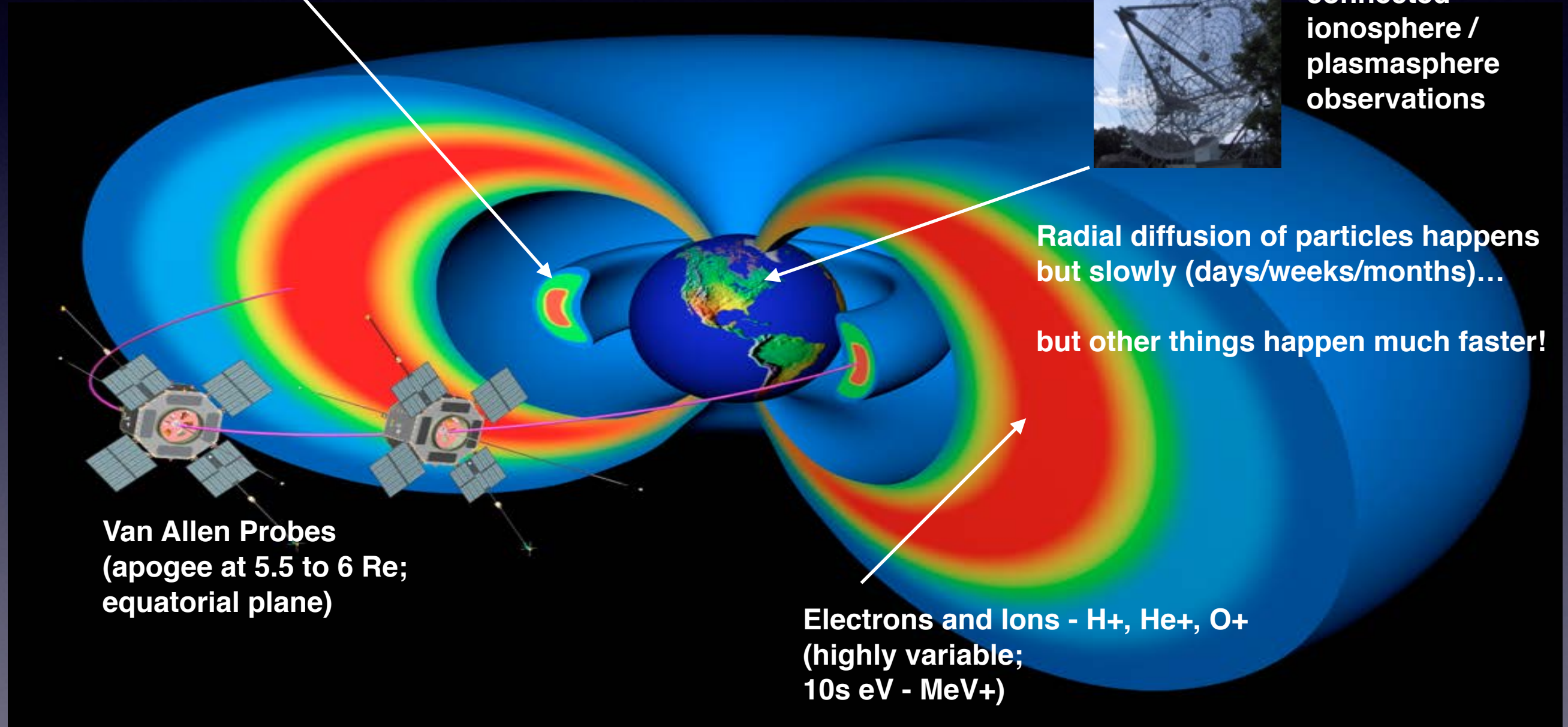
Fig. 7 Samples of E1 HEMP exposed regions for several burst heights. The *red circles* show the exposed regions for the given burst heights, for a nuclear burst over the central US (from Savage et al. 2010)

Earth's Radiation Belts

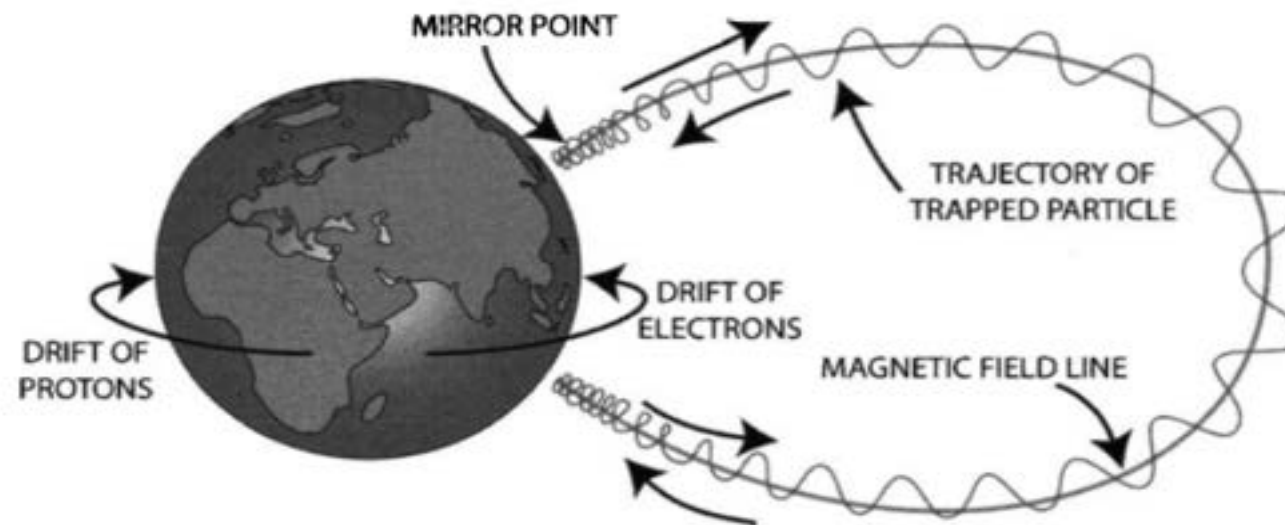
Protons (100+ MeV)
and HE electrons (100s keV)
(stable; Cosmic ray albedo neutron decay)



Magnetically
connected
ionosphere /
plasmasphere
observations



Particle Invariants



Characteristic time scales:

- Gyro: ~millisecond
- Bounce: ~0.1 - 1.0 s
- Drift: ~1 - 10 minutes

- Three types of periodic motion of trapped particles
 - gyro motion
 - bounce motion
 - drift motion
- Each motion has an associated adiabatic invariant

Spjeldvik and Rothwell, 1989

(D. Baker; W. Johnston GEM tutorial)

Artificial Radiation Belts

Starfish Prime
9 July 1962



Telstar 1
Bell Systems
launched 10 July 1962
failure early 1963

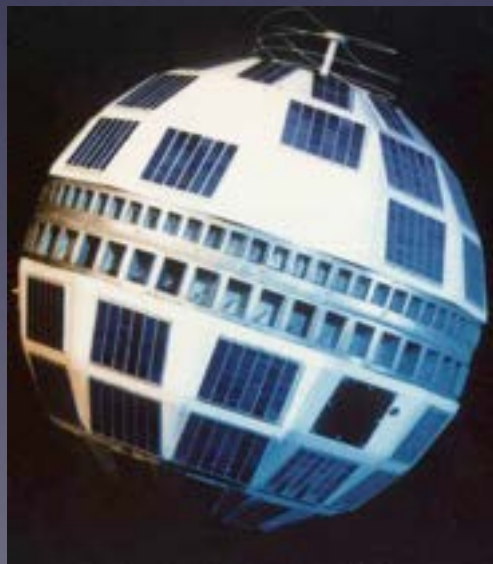
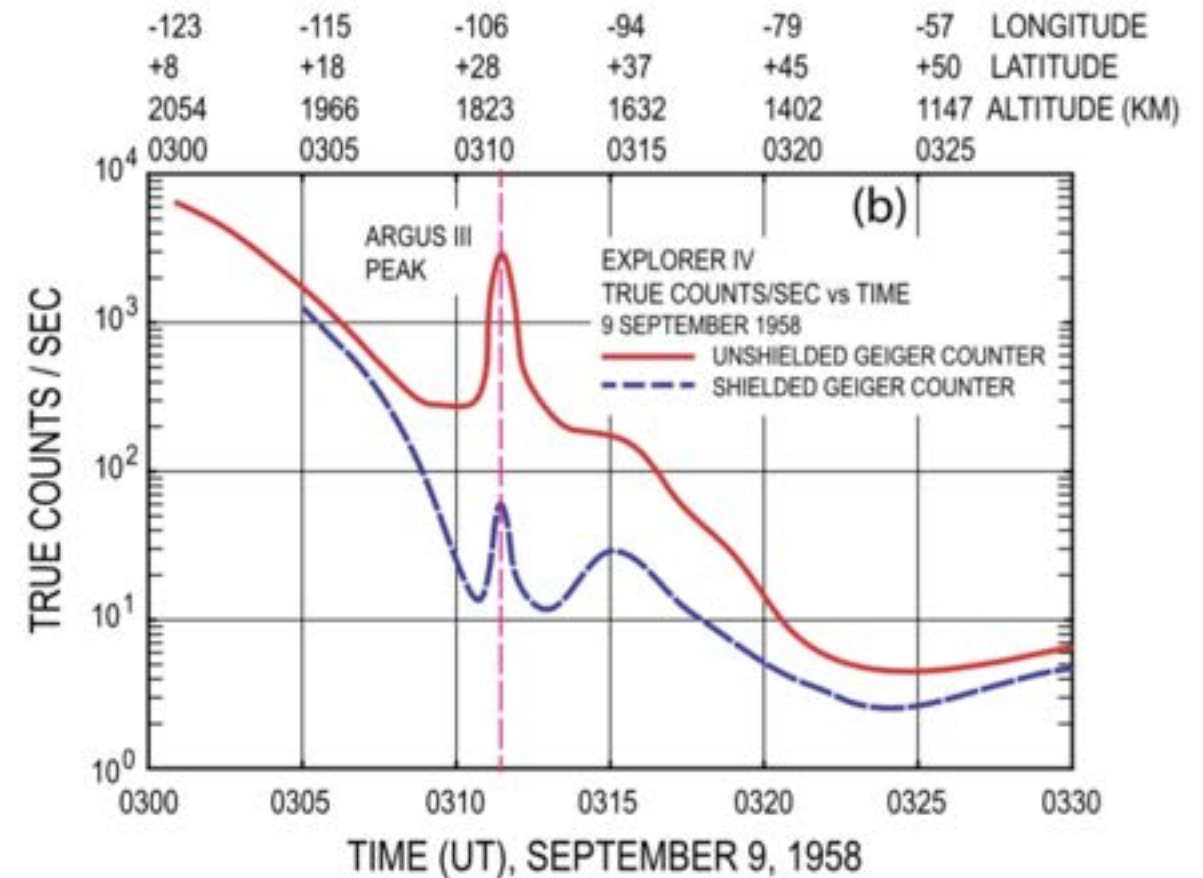
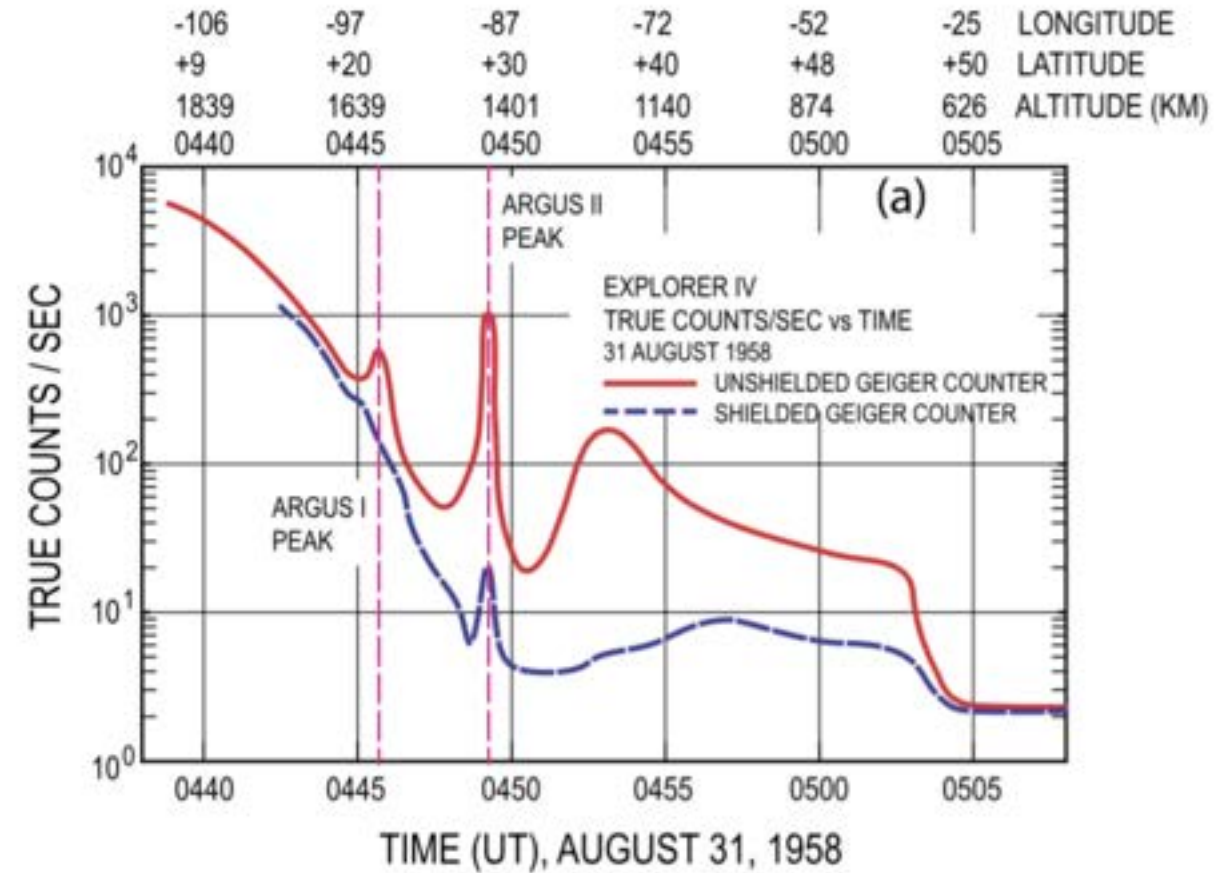


Fig. 10 Plots of passes by the Explorer IV satellite through the enhanced energetic electron fluxes in the artificial radiation belts created by the Argus nuclear explosions. (a) A pass through the Argus II belt, with the decaying Argus I belt still visible on 31 August 1958. (b) A pass through the Argus III artificial belt on September 6, 1958 (from Van Allen et al. 1959c)



Artificial Radiation Belts: Long Term Effects

Fig. 11 The decay of energetic electron fluxes in the artificial radiation belt created by the Argus III nuclear explosion, observed by the Explorer IV satellite over several weeks. The plot shows the product of the maximum true counting rate at the center of the Argus III shell with the geometric width of the shell at half maximum, to provide a measure of the electron content of the belt and its decrease with time (from Van Allen et al. 1959c)

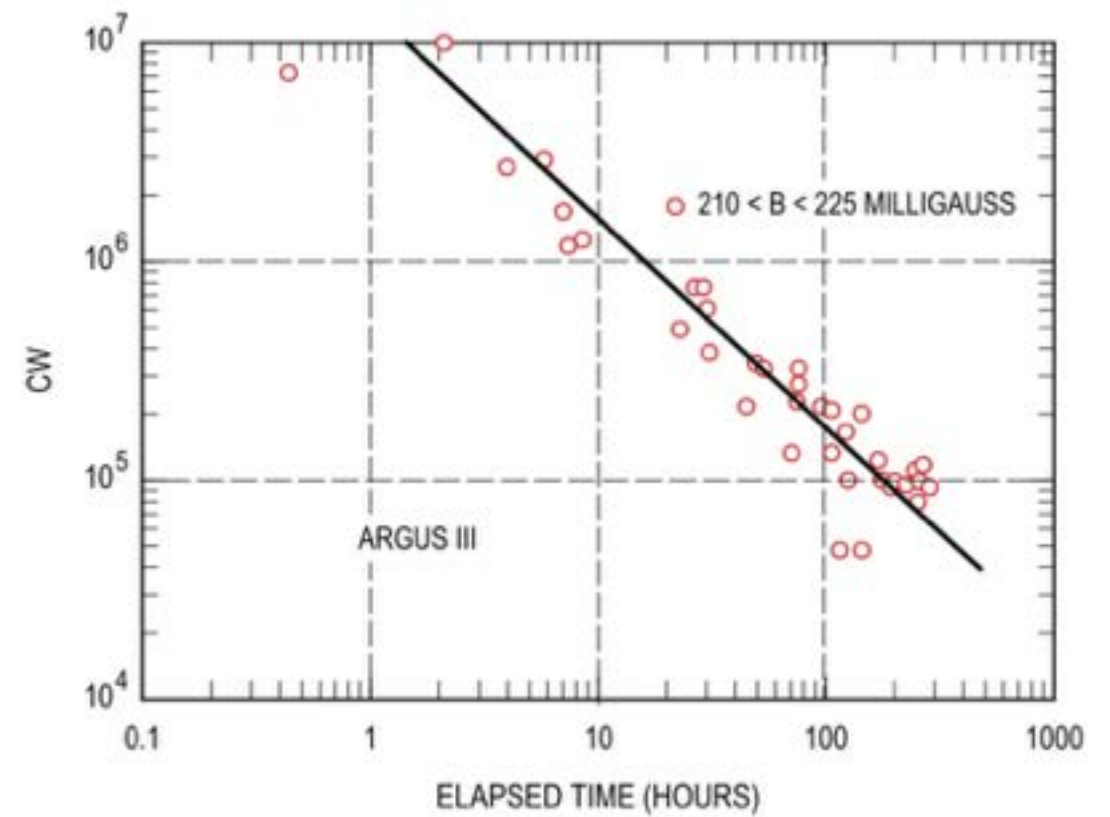


Fig. 14 The omnidirectional counting rate between the launch of Telstar-1 and the first of the Soviet high altitude blasts on day 295. The curves show the counting rates in a narrow λ ranges on individual L shells, close to the equator for $L = 1.7$ and increasingly larger l values for the higher L shells. The clustering of observational points is due to the precession of the Telstar-1 orbit (from Brown 1966)

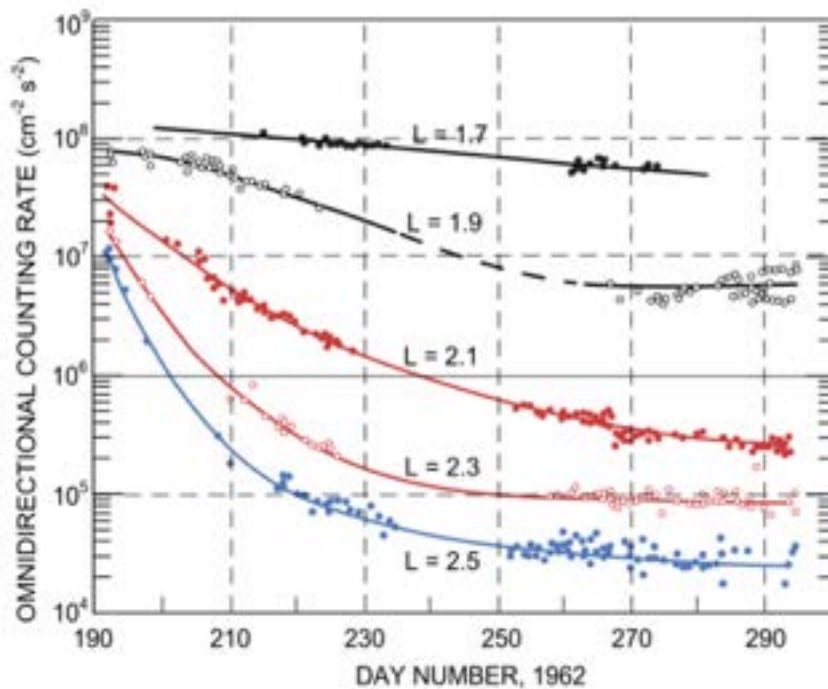
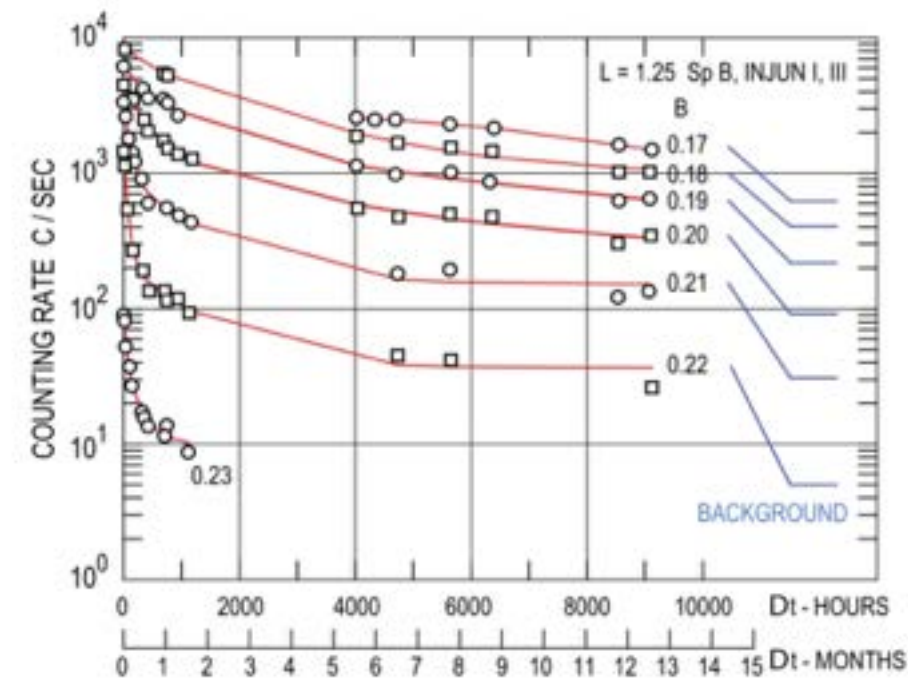


Fig. 16 The long-lasting energetic electron fluxes at $L = 1.25$, measured first by the Injun-I satellite in the aftermath of the Starfish detonation and, from its launch on December 13, 1962, by the Injun-III satellite. After the initial fast decay, fluxes in the artificial radiation belt stabilized and decayed over many months. Similar instruments on the two satellites responded to electrons between 1.5 and 5 MeV (from Van Allen 1964)



>5 MeV
relativistic
electron
fluxes

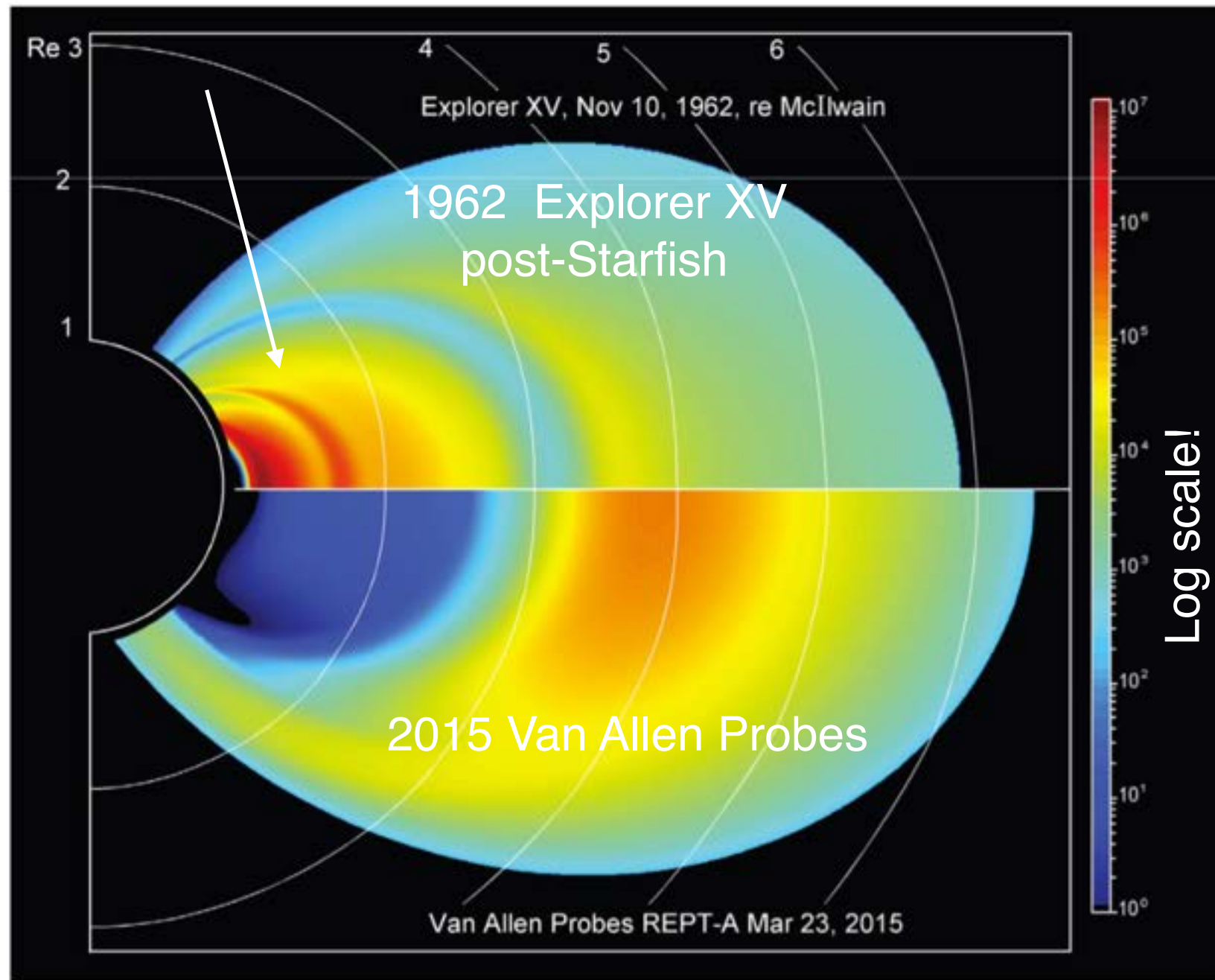


Fig. 21 Comparison of Explorer XV data from 10 November 1962 with Van Allen Probes data taken with the Relativistic Electron-Proton Telescope (REPT) on 23 March 2015. The Explorer XV data are adapted from McIlwain (1963) (see Fig. 20) and the Van Allen Probes data are adapted from measurements described in Baker et al. (2016). It is noted that the March 2015 outer zone fluxes of $E > 5$ MeV electrons were more intense and broader in spatial extent than were such electrons in the November 1962 case. On the other hand, the inner zone electron fluxes in the 1962 post-Starfish era were at least 10 million times more intense than fluxes seen in the present-day magnetosphere. Such high fluxes were deadly to orbiting spacecraft of the early 1960s (as described in the text)



Artificial Radiation Belts: Satellite Electronics Damage

Fig. 28 (a) Deterioration of transistor performance measured on Telstar-1. These were specially instrumented "damage-transistors" for the purpose of observing the nature and magnitude of radiation damage (from Fig. 30, Brown and Gabbe 1963). (b) Comparison of the radiation damage to transistors and solar cells. Solar cells are more rugged, but spacecraft are linearly dependent on the power supplied by the cells, whereas circuits can be designed to be radiation resistant by taking into account the degradation in transistor parameters. For today's spacecraft, solar cells remain critical, but the design and fabrication of electronic components have developed very significant radiation resistance (from Brown et al. 1963)

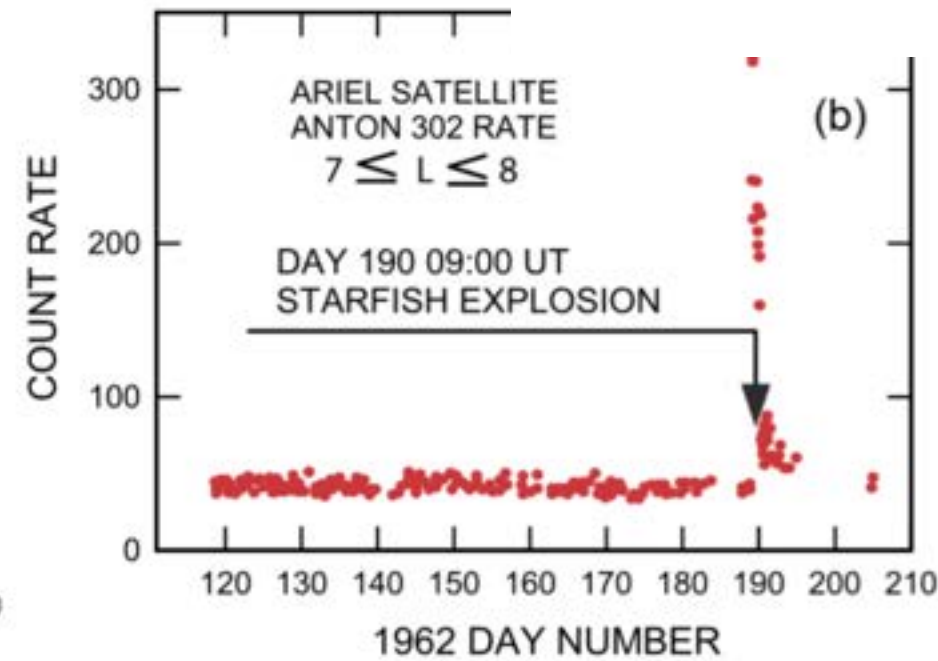
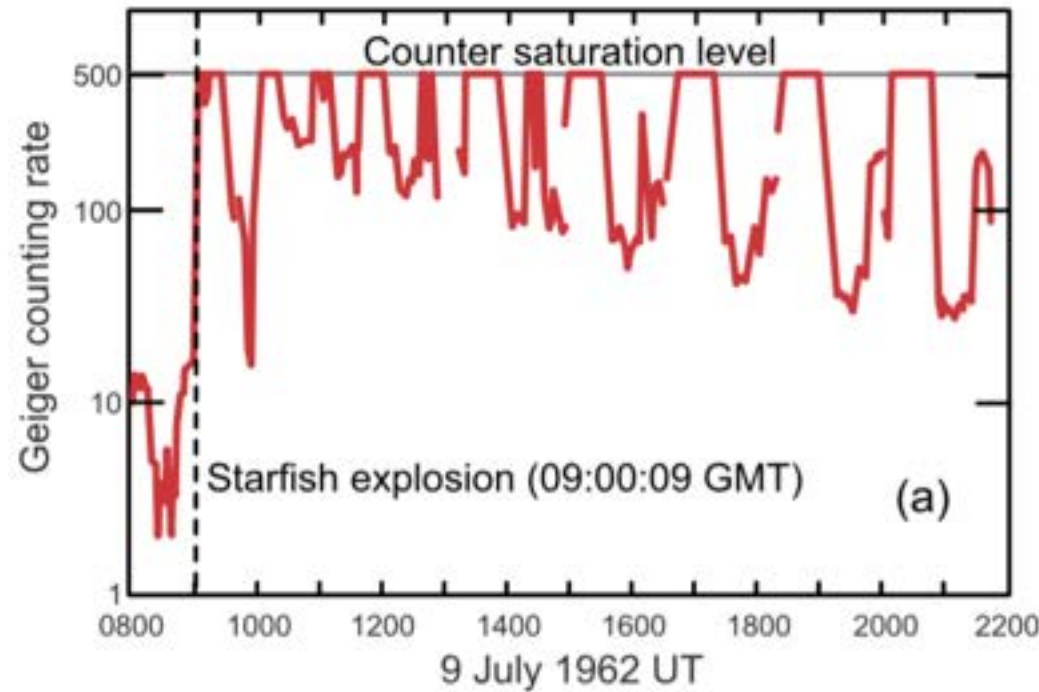
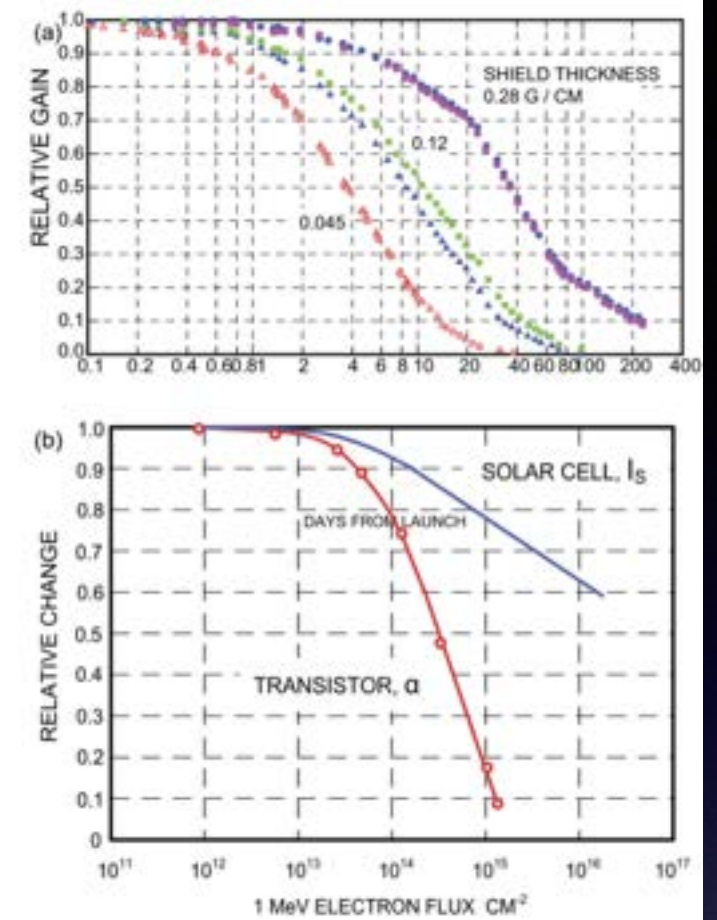


Fig. 23 (a) The Geiger counting rate observed on the Ariel-1 satellite. In the hours following the explosion the instrument regularly saturated on each orbit as the spacecraft crossed the forming artificial radiation belt. (b) In the long term observations of the stable high energy cosmic rays by Ariel-1, the high energy electrons injected by the explosion stand out even at high value L -shells (Figs. from Durney et al. 1962 and Elliot 1966)

Artificial Radiation Belts: Solar Cell Damage

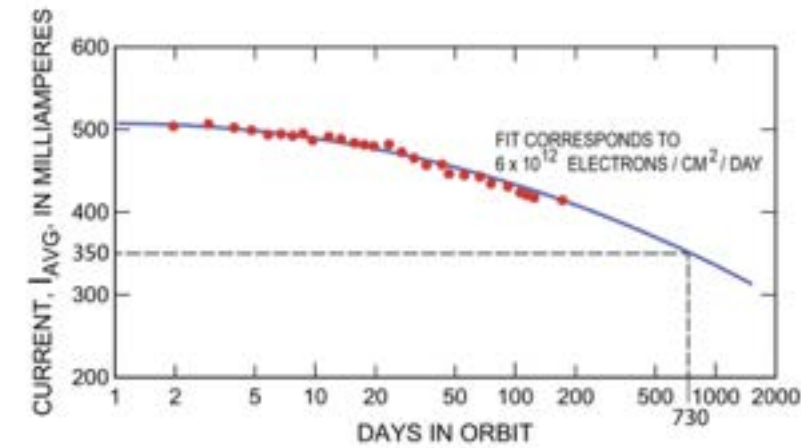


Fig. 27 The evolution of the average output of the current supplied by the solar cells on Telstar from launch to February 1963, corrected for mean solar distance. The fit corresponds to the damage calculated for a mission-averaged 1 MeV equivalent energetic electron flux rate of 6×10^{12} electrons cm^{-2} per day. The fit has been extrapolated to two years in orbit at the same energetic particle flux rate; the power output would then be reduced to 68% of its initial performance. (Taken from Fig. 28, Brown and Gabbe 1963)

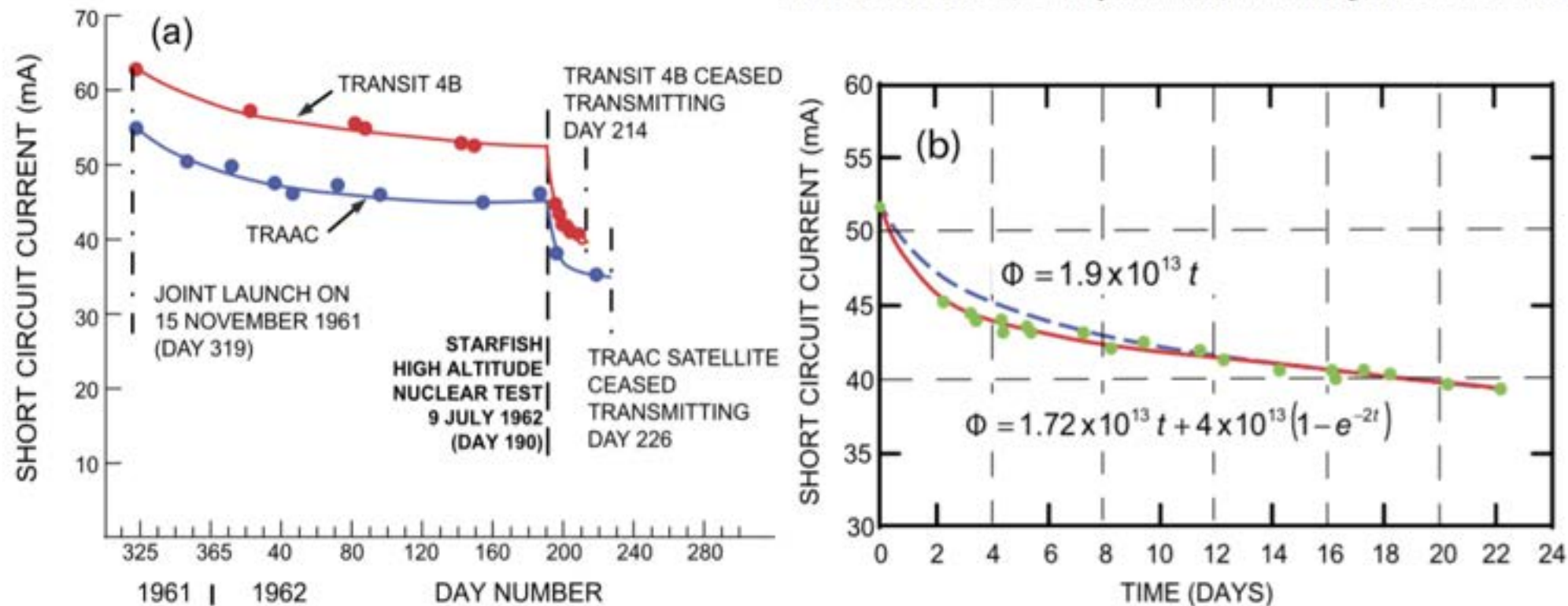


Fig. 24 Observation of the decreasing power from the solar cells on the TRAAC and Transit-4B satellites. (a) Time history from launch, showing the gradual damage from the natural radiation environment, followed by the much accelerated loss of power after the Starfish explosion (from Fig. 5 in Fischell 1962a). (b) Transit-4B solar-panel performance after the Starfish event, showing that the performance loss is best modeled by an initial period of higher intensity radiation, followed by a constant radiation flux (from Fig. 7 in Fischell 1962a)

Artificial Radiation Belts: Global Magnetometer Effects

Fig. 31 Magnetograms from six stations distributed in distance from Johnston Island following the Argus III nuclear detonation on September 6, 1958. It shows two groups of signatures; the first very prompt, the second showing reasonably clear velocity dispersion. The fitted velocities are by Berthold et al. (1960); for the prompt signal, Caner (1964) argued that it was arguably synchronous worldwide, as was later found for the prompt signature from Starfish

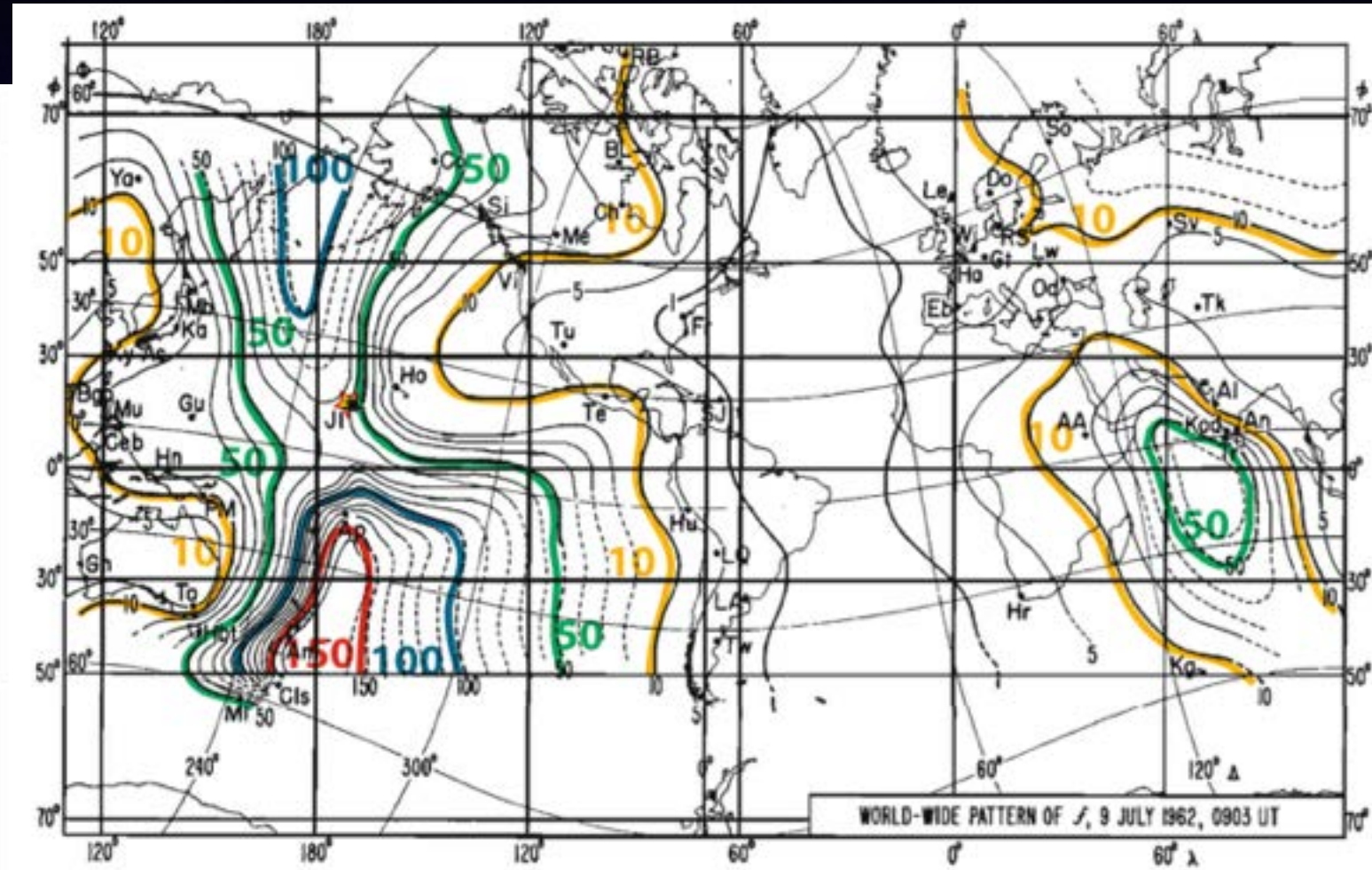
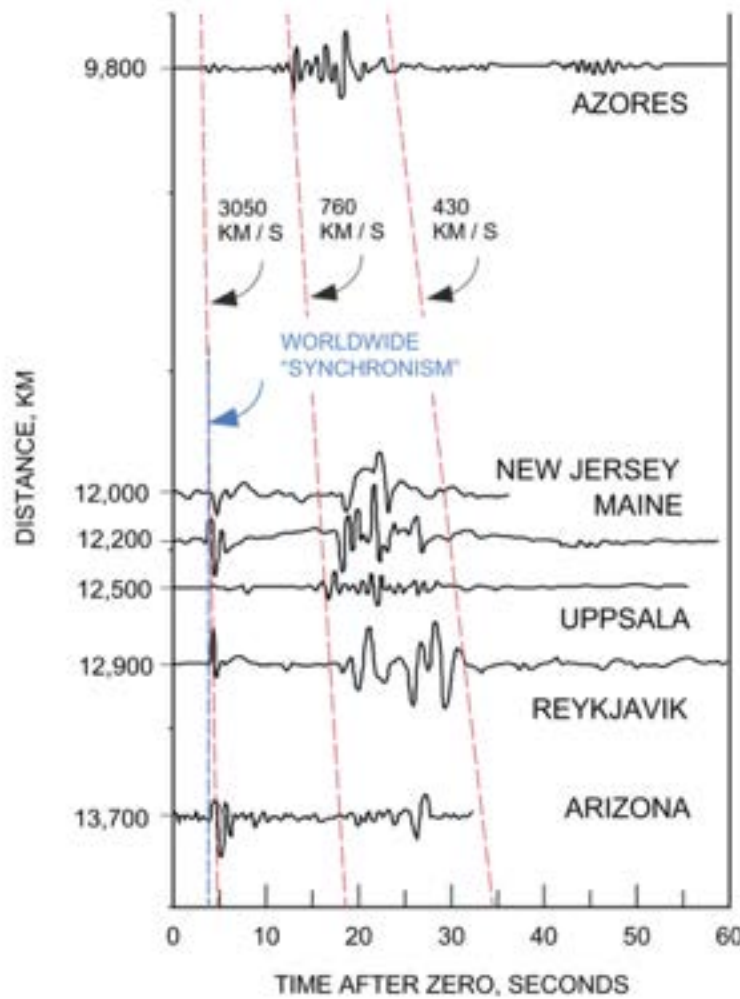


Fig. 34 Isopleths of the amplitude of the total-disturbance magnetic vector at 0903 UT on July 9, 1962 (2 min 51 s after Starfish), plotted on a Mercator projection. The detonation took place 400 km above Johnston Island (JI). Values are in gammas. A contour interval of 10 gammas is used from the 10-gamma isopleth upward; the color lines are 10, 50, 100, and 150 gammas (from Bomke et al. 1966)

Human triggered events can be obvious.



Fig. 1 From *left to right*, the Orange, Teak, Kingfish, Checkmate, and Starfish high-altitude nuclear tests conducted in 1958 and 1962 by the United States near Johnston Island in the mid-Pacific (from Foster et al. 2008)

.. but there are also unexplained natural space weather effects that might be human related.

Wave-Particle Interactions

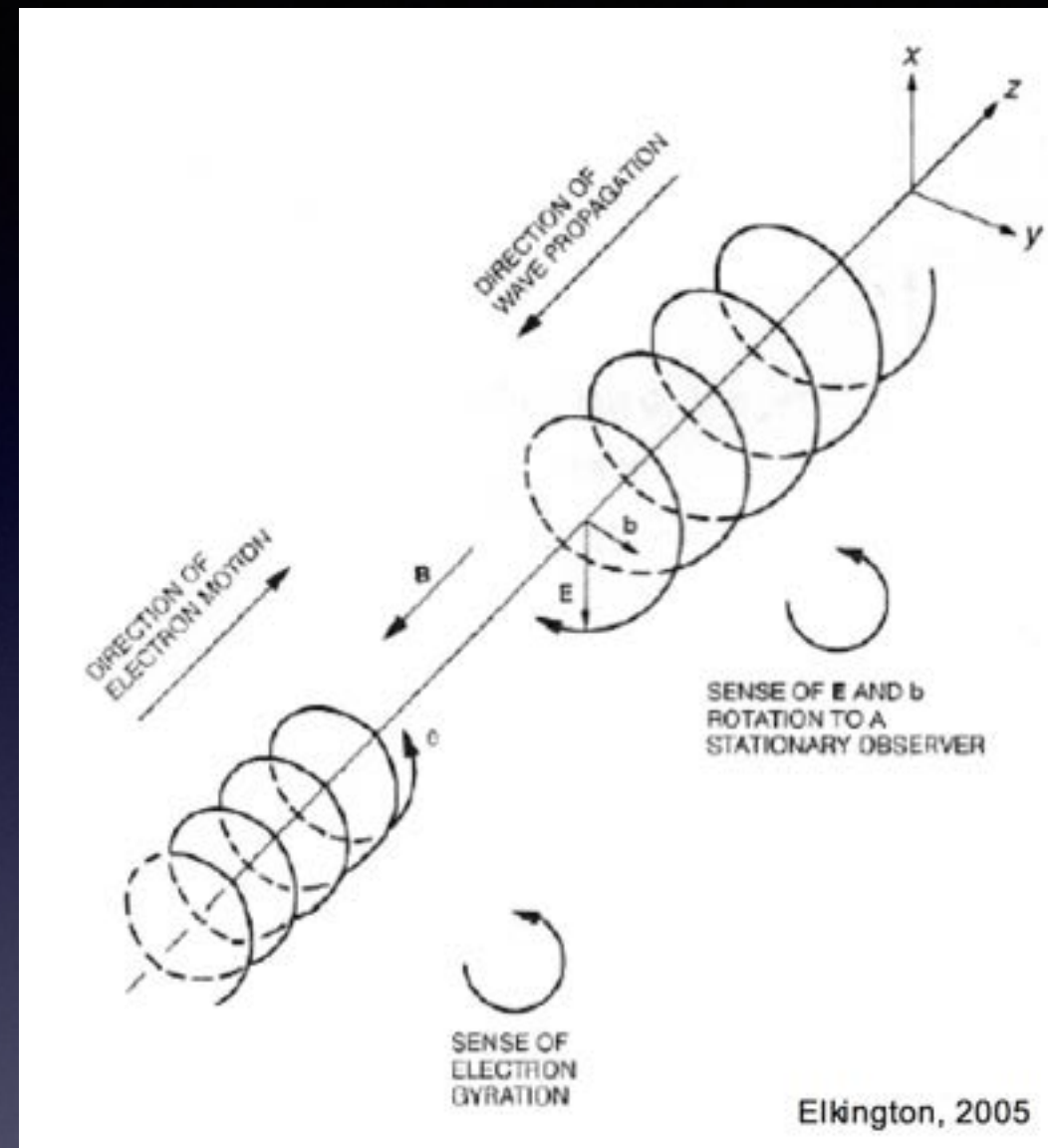
A zoo of natural waves exists in the plasma within our magnetosphere:

- Chorus / Whistlers
- ULF waves
- Magnetosonic waves
- EMIC waves
- Plasmaspheric Hiss [incoherent]

Some can be affected by human transmissions.

These waves can greatly affect nearby particles (acceleration, loss).

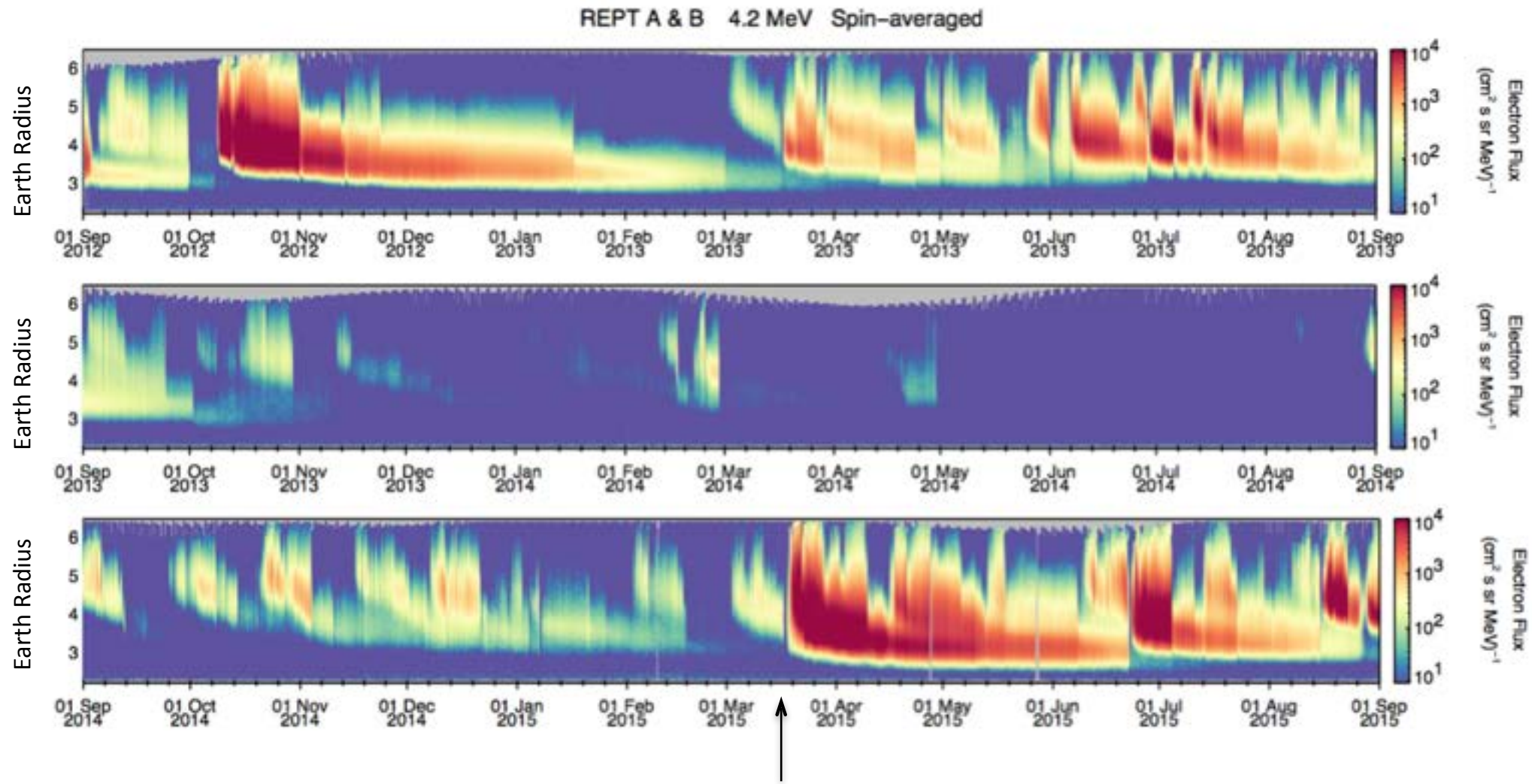
Resonance conditions can depend on things like the ambient background plasma (e.g. local natural space weather)



Pitch angle, Coulomb scattering = Loss
Slow diffusion = Transport
Linear and **non-linear** processes involved

The 'Impenetrable Barrier' to Radiation Belt Electrons

Van Allen Probes: Three Years' Observations of Ultra-Relativistic Electrons



17 March 2015

A mystery... or is it?

Baker et al, 2014

VLF Transmitters

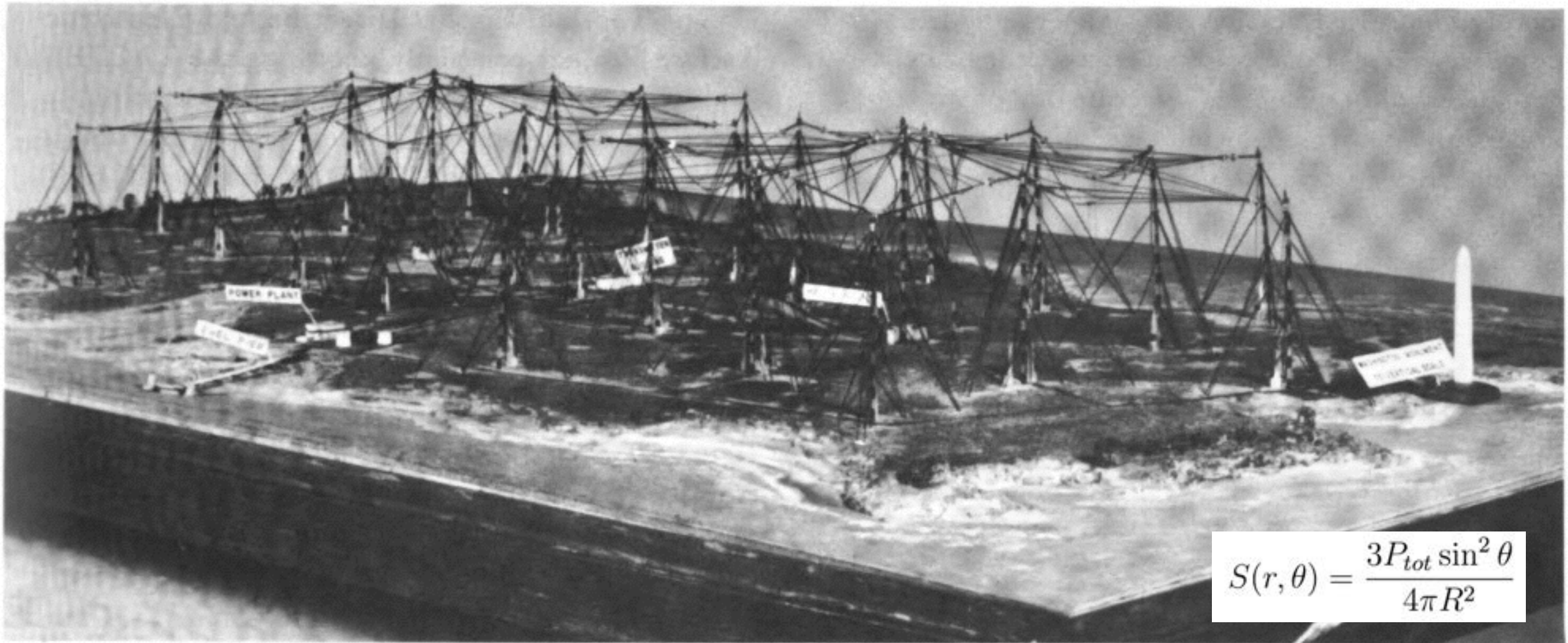


Figure 5. Antenna system of VLF transmitter, Cutler, Maine.

VLF Transmitters

Table 2. VLF Transmitter Call Signs, Frequency, Geographic Coordinates, Output Power, and Geomagnetic *L* Shells

Transmitter	Frequency (kHz)	Latitude	Longitude	Estimated Power (kW)	<i>L</i> Shell (2008)
NRK, Iceland	37.5	63° 51' N	22° 28' W	100	5.5
NLK, Seattle	24.8	48° 12' N	121° 55' W	250	2.9
NDK, North Dakota	25.2	46° 22' N	98° 20' W	500	3.3
NAA, Maine	24.0	44° 39' N	67° 17' W	1000	2.9
GQD, Anthorn	22.1	54° 53' N	03° 17' W	60	2.7
HWU, Rosnay	22.6	46° 43' N	01° 15' E	200	1.8
DHO, Ramsloh	23.4	53° 05' N	07° 37' E	300	2.4
ICV, Tavolara Island	20.27	40° 55' N	09° 45' E	50	1.5
NWC, NW Cape	19.8	21° 49' S	114° 10' E	1000	1.4
NTS, Woodside	18.6	38° 29' S	146° 56' E	25	2.4
NPM, Hawaii	21.4	21° 26' N	158° 09' W	500	1.2
NAU, Puerto Rico	40.75	18° 25' N	67° 09' W	125	–
JAP, Ebino	22.2	32° 03' N	130° 50' E	100	1.2

(Rodger, 2009)

VLF and ELF Communications Signals: Naval Use

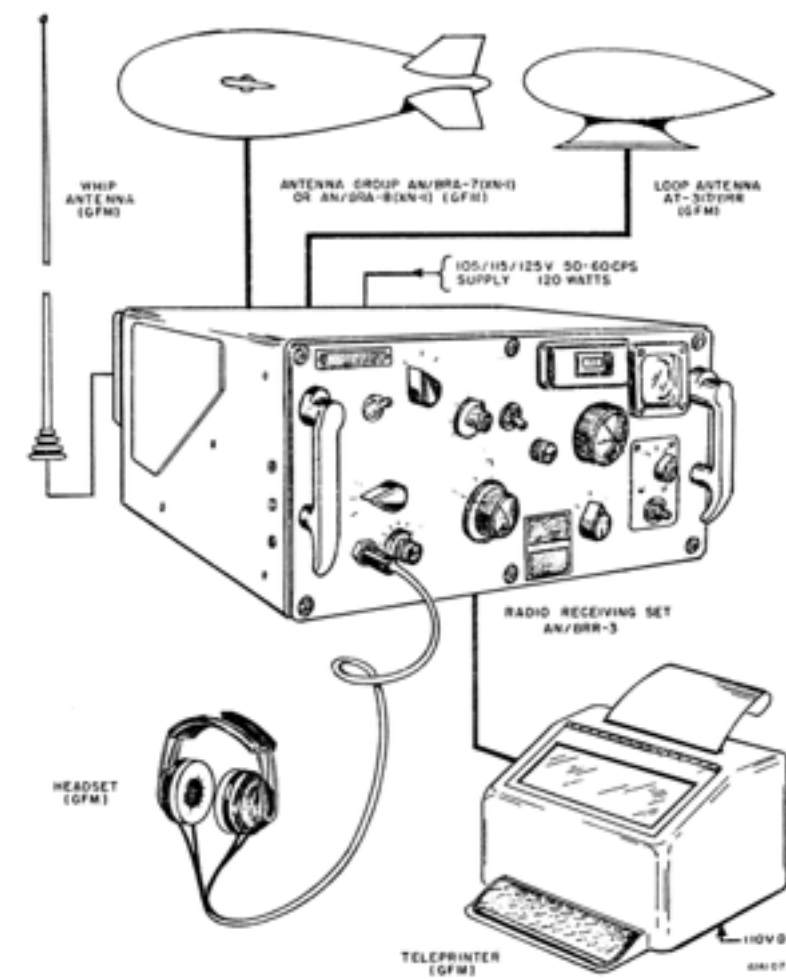
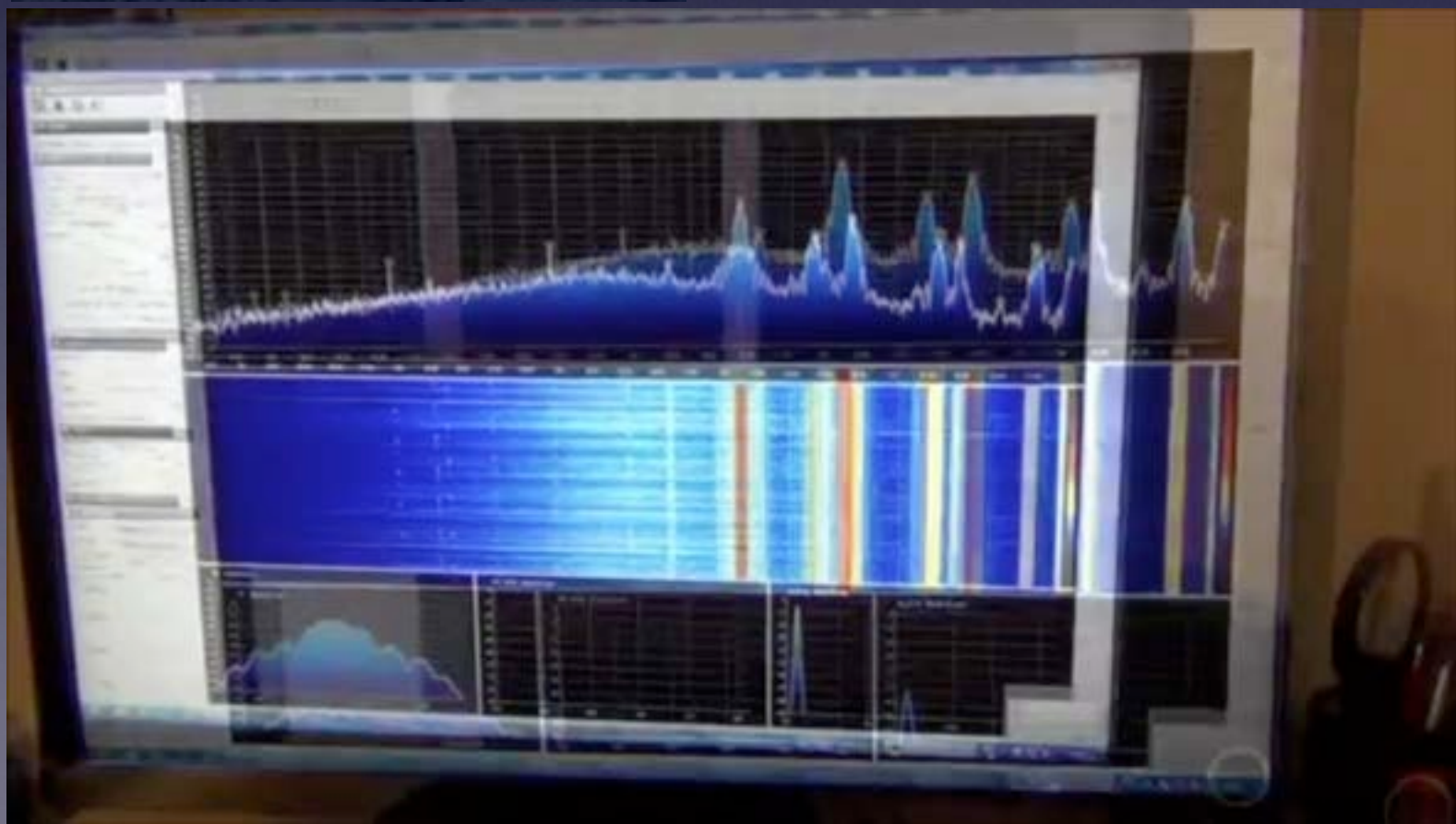


Figure 3-28. Radio Receiving Set AN/BRR-3 and Accessory Equipment (Typical)

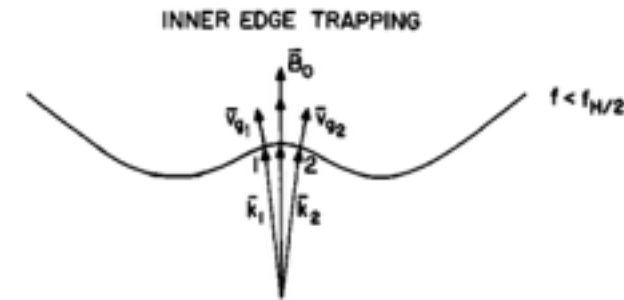


VLF Transmitters

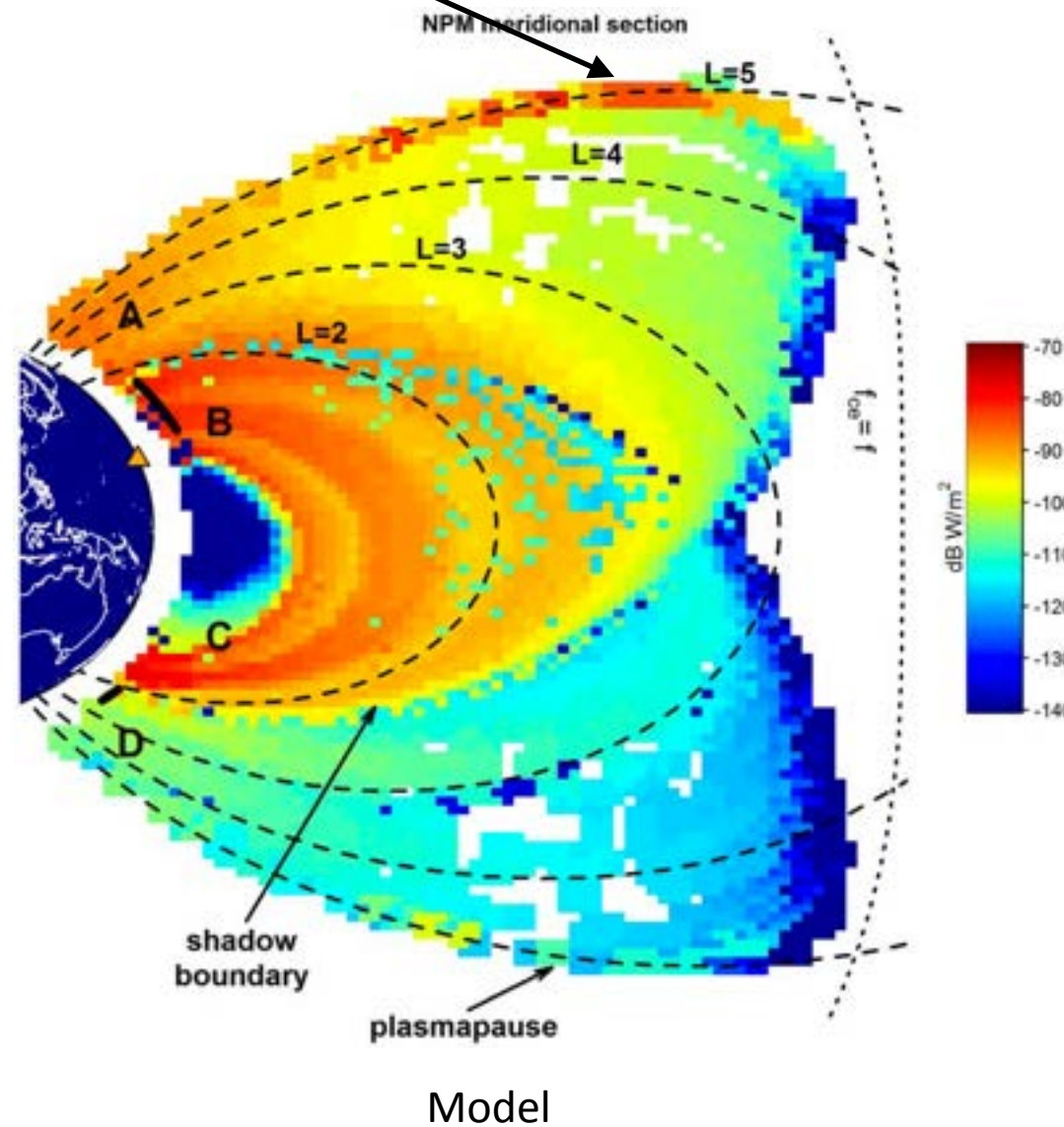
The large negative radial density gradients deflect the ray inward, but as the ray moves in and encounters markedly reduced gradients, the curvature of the earth's field deflects the ray outward. Upon entering the region of high gradient the ray will again be refracted inward, and the process will be repeated. The result is that the ray is trapped by the density gradient and its path oscillates about the direction of earth's field.

Gradient trapping
Helliwell, 1965

Inan and Bell, 1977

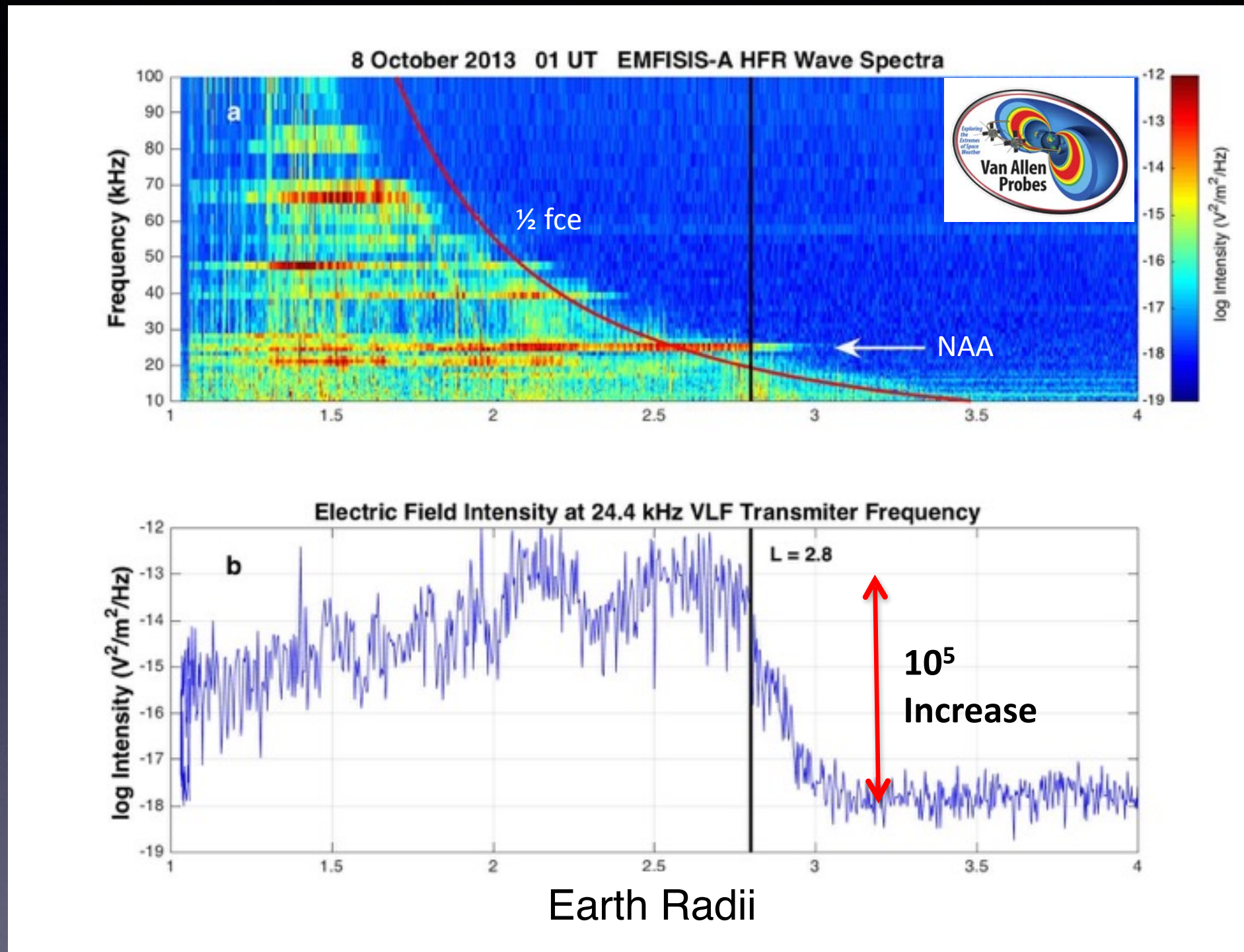


(L = magnetic coordinate)

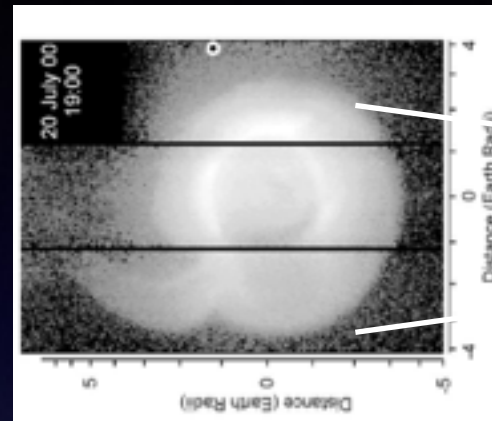
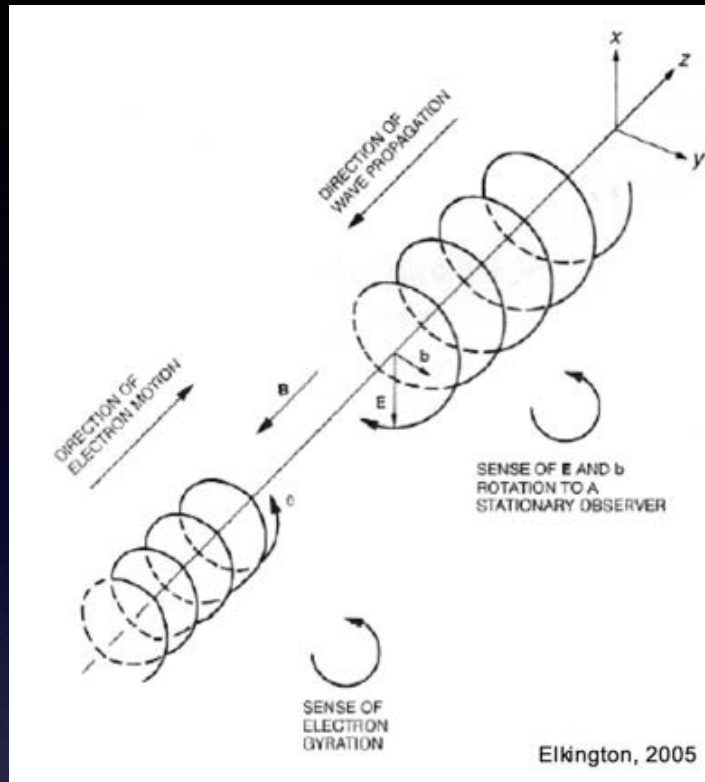


Meridional section of power flux predicted by AFRL's VLF Propagation Code in the plasmasphere due to NPM transmissions. The transmitter is marked by a triangle. Note the prominent shadow boundary in the conjugate hemisphere. An analogous boundary (not visible) exists in the transmitter hemisphere. [Starks et al, 2009]

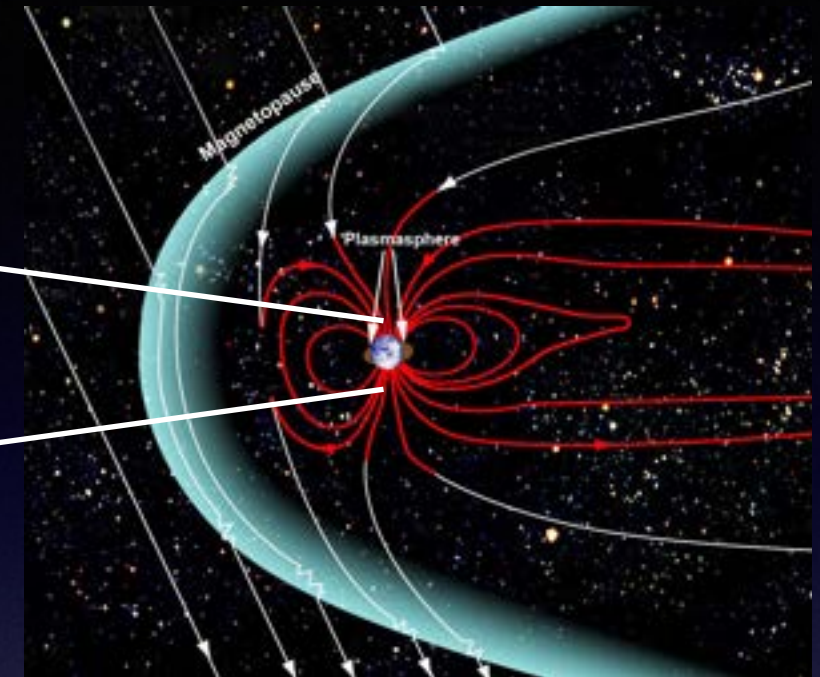
VLF Transmitters: In-situ Measurements



VLF Resonance with Radiation Belts?



Sandel et al
2001
IMAGE EUV
30.4 nm He+



The Plasmasphere

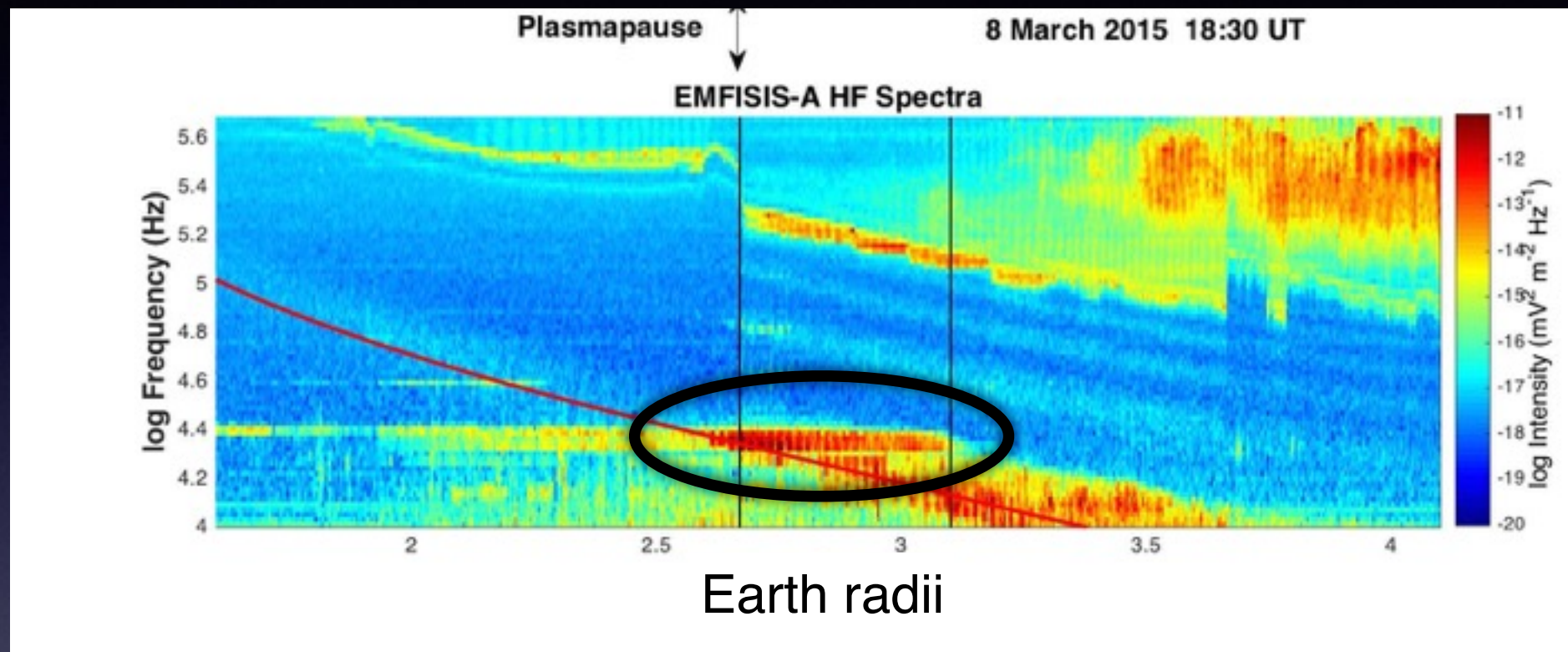
Note that 17.1 and 22.3 kHz VLF transmitter frequencies cannot resonate at the equator beyond [2.2 - 2.4 Earth radii], respectively...

Abel and Thorne 1998

But all these calculations done ONLY for some (not all) conditions.

No Nonlinear Effects were included.

VLF Transmitters Interact With Natural Whistler Waves



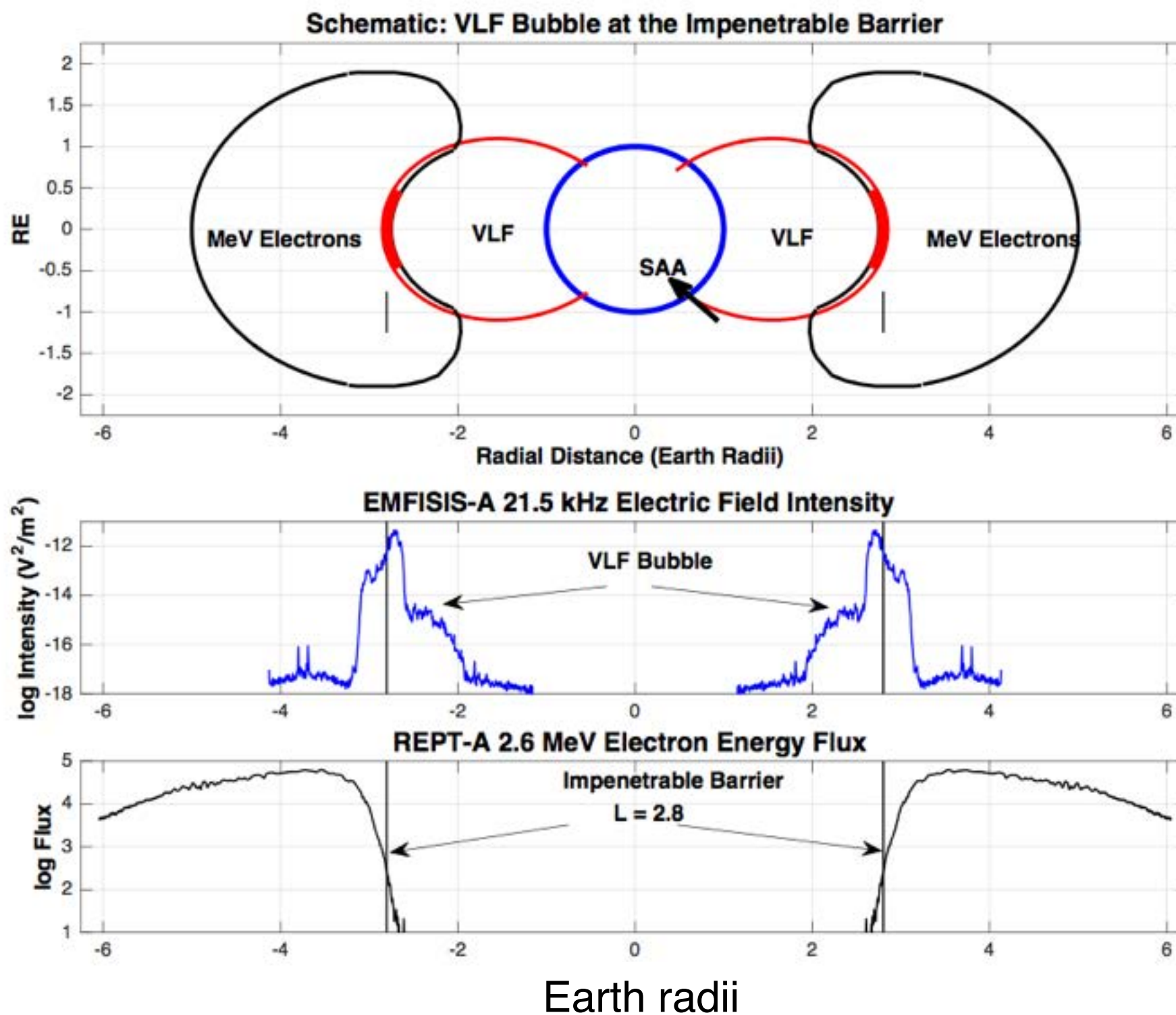
It is likely that VLF TX stimulates significant whistler wave growth outside the plasmasphere

e.g. Foster and Rosenberg, 1976

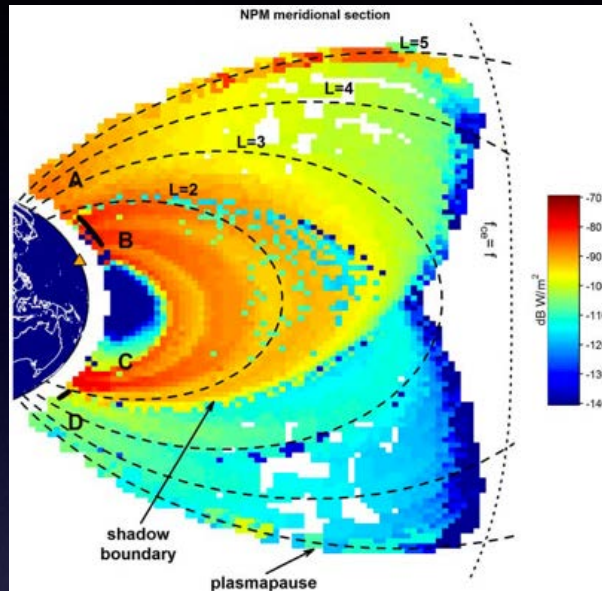
The VLF transmitter signal significantly increases in intensity as it encounters a band of natural wave emissions immediately beyond the plasmasphere.

This is strong enough to dump radiation belt electrons directly into the atmosphere (where they are scattered and lose their energy).

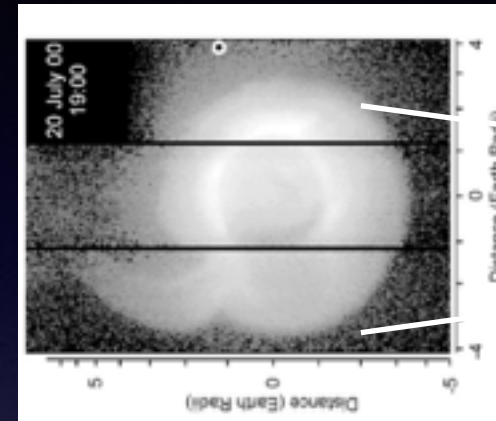
Barriers, Bubbles, and Plasmapause: The Big Picture



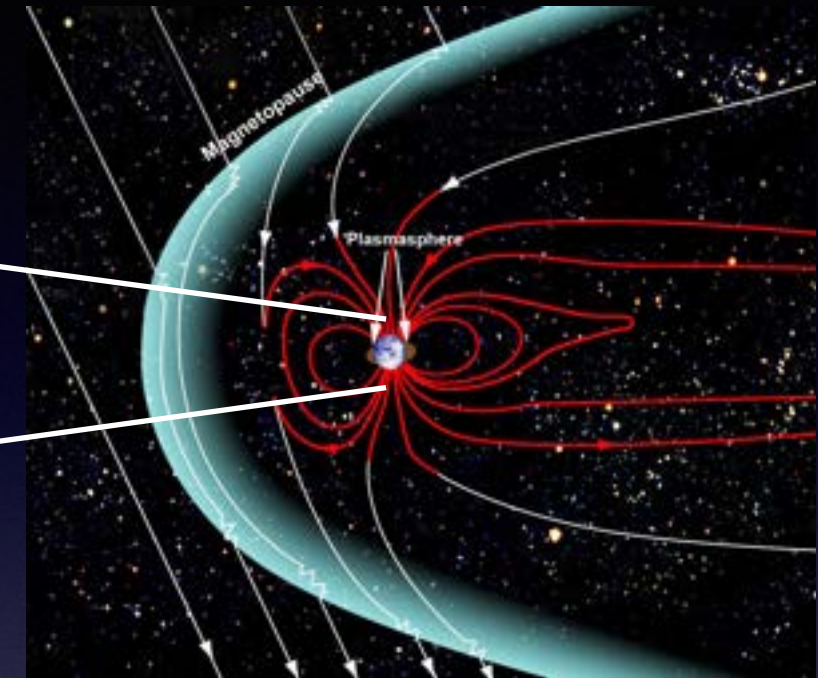
Conclusion / Connections to amateur radio



(VLF)



Sandel et al
2001
IMAGE EUV
30.4 nm He+



The Plasmasphere

All HF signals $>$ plasma frequency leak out of the plasmasphere. Although they are unlikely to modify the environment directly, they are an excellent probe of the ionospheric structure.

Radiation belts and other anthropogenic disturbances can be directly influenced by ionospheric / plasmaspheric conditions.

We should continue to find new ways to understand this environment - with amateur radio data help.